








# Testing Different Tectonic Models for the Source of the $M_w$ 6.5, 30 October 2016, Norcia Earthquake (Central Italy): A Youthful Normal Fault, or Negative Inversion of an Old Thrust?

L. Bonini<sup>1,2</sup> , R. Basili<sup>2</sup> , P. Burrato<sup>2</sup> , V. Cannelli<sup>2</sup> , U. Fracassi<sup>2</sup> , F. E. Maesano<sup>2</sup> , D. Melini<sup>2</sup>, G. Tarabusi<sup>2</sup> , M. M. Tiberti<sup>2</sup>, P. Vannoli<sup>2</sup>, and G. Valensise<sup>2</sup>

<sup>1</sup>Dipartimento di Matematica e Geoscienze, University of Trieste, Trieste, Italy, <sup>2</sup>Istituto Nazionale di Geofisica e Vulcanologia, Rome, Italy

## Key Points:

- We used a multidisciplinary, multistage approach to investigate the seismotectonic setting of the 2016,  $M_w$  6.5, Norcia earthquake
- We tested different models against geological, seismological, and geodetic data
- We find that the 30 October 2016,  $M_w$  6.5, Norcia earthquake was generated by the extensional reactivation of a major thrust fault

## Supporting Information:

- Supporting Information S1

## Correspondence to:

L. Bonini,  
lbonini@units.it

Accepted 7 FEB 2019

Accepted article online 11 FEB 2019

**Abstract** We adopted a multidisciplinary approach to investigate the seismotectonic scenario of the 30 October 2016,  $M_w$  6.5, Norcia earthquake, the largest shock of the 2016–2017 central Italy earthquake sequence. First, we used seismological and geodetic data to infer the dip of the main slip patch of the seismogenic fault that turned out to be rather low-angle ( $\sim 37^\circ$ ). To evaluate whether this is an acceptable dip for the main seismogenic source, we modeled earthquake deformation using single- and multiple-fault models deduced from aftershock pattern analyses. These models show that the coseismic deformation generated by the Norcia earthquake is coherent with slip along a rather shallow-dipping plane. To understand the geological significance of this solution, we reconstructed the subsurface architecture of the epicentral area. As the available data are not robust enough to converge on a single fault model, we built three different models encompassing all major geological evidence and the associated uncertainties, including the tectonic style and the location of major décollement levels. In all models the structures derived from the contractional phase play a significant role: from controlling segmentation to partially reusing inherited faults, to fully reactivating in extension a regional thrust, geometrically compatible with the source of the Norcia earthquake. Based on our conclusions, some additional seismogenic sources falling in the eastern, external portions of the Apennines may coincide with inherited structures. This may be a common occurrence in this region of the chain, where the inception of extension is as recent as Middle-Upper Pleistocene.

## 1. Introduction

The 24 August 2016,  $M_w$  6.0, Amatrice, central Italy, shock (hereinafter *Amatrice earthquake*) marked the beginning of a long and destructive normal faulting earthquake sequence. It was followed by an  $M_w$  5.9 shock on 26 October 2016, near Visso, and by an  $M_w$  6.5 shock on 30 October 2016, near Norcia (hereinafter *Norcia earthquake*), the largest of the entire sequence (Figure 1). On 18 January 2017 four additional shocks in the  $M_w$  range of 5.2 to 5.5 struck the region around Campotosto, halfway between Amatrice and the city of L'Aquila, the locus of the catastrophic 6 April 2009,  $M_w$  6.3 earthquake. All in all, over 80,000 events illuminated a nearly 75-km-long fault system running along the axis of the central Apennines, an orogenic belt currently undergoing extension.

Although the 2016–2017 central Italy earthquakes occurred 2 years ago, they have already been investigated by numerous scientists worldwide, probably due to the severity of the damage they caused, to their source complexity, and to the spectacular surface breaks generated by the largest shocks (e.g., Bonini, Maesano, et al., 2016; Cheloni et al., 2017; Chiaraluce et al., 2017; Civico et al., 2018; Doglioni et al., 2016; Falcucci et al., 2018; Pizzi et al., 2017; Porreca et al., 2018; Pucci et al., 2017; Walters et al., 2018; Xu et al., 2017; Zhong et al., 2018; see also references in Tables 1 and 2). Most activated surface faults exhibit a steep dip angle (e.g., Villani et al., 2018), although aftershock patterns, focal mechanisms, and geodetic data analyses all suggest a rather low dip for the causative fault of the Norcia mainshock ( $40^\circ$  on average; see Table 1).

The epicentral area of the Norcia earthquake lies in the hanging wall of the Sibillini thrust, one of the most prominent contractional structures of the Central Apennines (Figure 1). It is well established in the

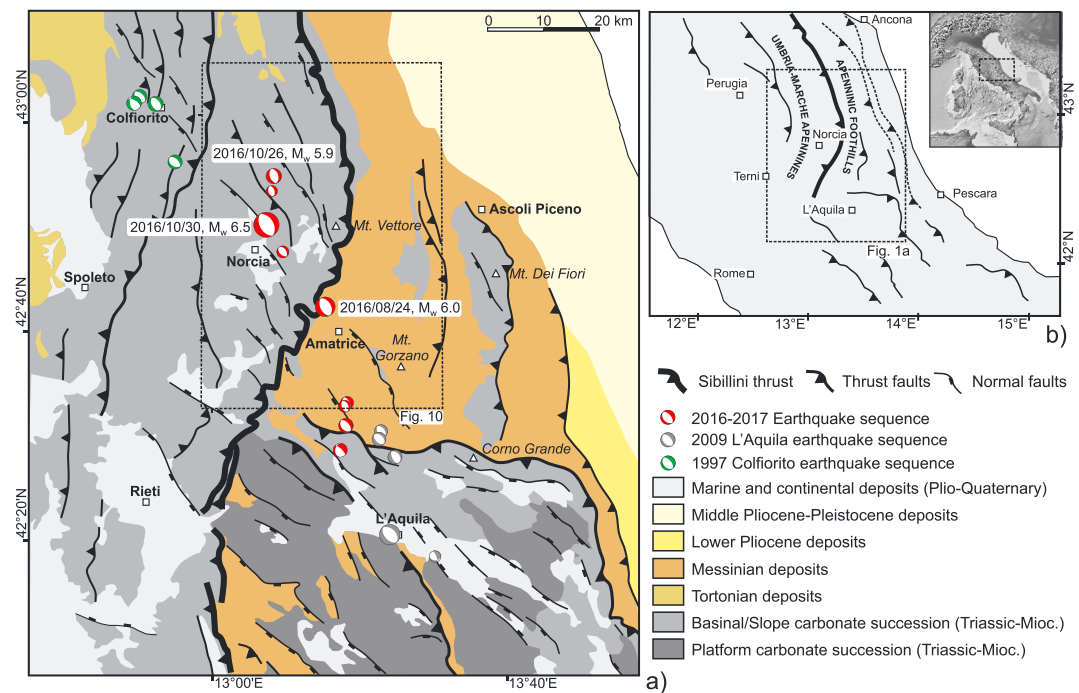


**Figure 1.** (a) Tectonic map of the region hit by the 2016/2017 central Italy earthquakes and surroundings, showing the focal mechanism of the largest events of the sequence and of other recent earthquakes (all are color-coded). Tectonic features are modified from Di Domenica et al. (2014); the focal mechanisms are from Chiaraluce et al. (2017). (b) Simplified tectonic sketch of the central-northern Apennines.

literature that young extensional regimes may reuse inherited structures during their early phases (e.g., Salazar-Mora et al., 2018). As extension is a somewhat recent occurrence along the most external portion of the Apennines, partial or total reuse of inherited thrust faults is indeed a viable scenario. In this respect, the rather shallow dip suggested by the majority of published studies for the main earthquake causative fault must be considered carefully, because it may imply the inherited structures played a prominent role, as already suggested by other investigators (e.g., Bonini, Maesano, et al., 2016; Chiarabba et al., 2018; Falcucci et al., 2018; Scognamiglio et al., 2018).

In the first part of this study, we analyzed the geodetic data to infer the dip of the main earthquake causative fault, with the aim to confirm or dispute previous estimates (Table 1). We then used our best fitting dip to build a model based on Differential Interferometric Synthetic Aperture Radar (DInSAR) and Global Positioning System (GPS) data. The model was used to derive a slip distribution for all faults that can be imaged by aftershock distributions and hence to test if our solution fits satisfactorily other independent data (e.g., the rake of slipped fault patches).

In the second part of the study, we reconstructed the subsurface architecture of the upper crust in the epicentral area to shed light on the tectonic evolution of the earthquake causative faults. Unfortunately, our knowledge of subsurface data is affected by uncertainties, which did not allow us to converge on a single, well-constrained solution. To overcome this limitation, we built different tectonic models encompassing the major uncertainties in our geological understanding of the area. Finally, we discussed the seismotectonic implications of each model and compared our findings with those proposed so far in the literature.

## 2. Geological Setting

The 2016–2017 earthquakes occurred in the Umbria-Marche Apennines and their foothills (Figure 1). The stratigraphy and structural features of this area have been the subject of thorough investigations for decades

**Table 1**  
*Fault Parameters Calculated for the 30 October 2016 Earthquake*

INGV parameters	Lon (°)	Lat (°)	Depth (km)	M <sub>w</sub>									
	13.1107	42.8322	9.2	6.5									
Author	Lon_Mec	Lat_Mec	Depth_Mec	Mw_Mec	StrikeA (°)	DipA (°)	RakeA (°)	StrikeB (°)	DipB (°)	RakeB (°)	Double couple (%)	CLVD (%)	Method
GCMT <sup>a</sup>	13.16	42.75	12	6.6	154	37	-96	342	53	-85	-	-	CMT algorithm incorporating intermediate-period surface waves
INGV-TDMT <sup>b</sup>	13.1102	42.8398	5	6.5	151	47	-89	330	43	-91	68	32	Time Domain moment Tensor (waveform inversion)
INGV - RCMT <sup>c</sup>	13.16	42.78	10	6.6	155	37	-98	345	53	-84	-	-	CMT modified algorithm (modeling intermediate-period surface waves)
SLU MT <sup>d</sup>	-	-	2	6.33	150	55	-90	330	35	-90	82	18	Broadband waveform inversion of ground velocities in the 0.02-0.10 Hz frequency band
USGS <sup>e</sup>	-	-	15.5	6.6	162	27	-84	335	63	-93	82	-	W-phase Moment Tensor (Mww)
GFZ-1 <sup>f</sup>	13.13	42.92	10	6.5	158	44	-88	337	46	-90	-	-	GEOFON standard inversion using body and surface waves
GFZ-2 <sup>f</sup>	13.14	42.92	10	6.5	152	44	-94	338	46	-84	-	-	GEOFON W-Phase solution
IPGP <sup>g</sup>	-	-	8	6.5	165	36	-80	332	54	-98	-	-	SCARDEC teleseismic body waves
Walters et al. (2018)	-	-	3	6.6	161	34	-81	-	-	-	-	-	Teleseismic long-period body waves inversion
Zhong et al. (2018)	-	-	4	6.58	165	32	-90	-	-	-	66	-	GPS waveforms inversion using the gCAP method
Zhong et al. (2018)	-	-	5	6.54	163	58	-90	-	-	-	69	-	Broadband waveforms inversion sampled to 10 Hz frequency
Zhong et al. (2018)	-	-	4	6.54	161	33	-90	-	-	-	71	-	Joint GPS and broadband waveforms inversion

*Note.* CLVD, compensated linear vector dipole; CMT, centroid moment tensor; GPS, Global Positioning System.

Key to individual data sources:

<sup>a</sup><http://www.globalcmt.org>, <sup>b</sup><http://cnt.rm.ingv.it/>, <sup>c</sup><http://www.bo.ingv.it/RCMT>, <sup>d</sup><http://www.eas.slu.edu>, <sup>e</sup><https://earthquake.usgs.gov>, <sup>f</sup><https://geofon.gfz-potsdam.de>, <sup>g</sup><http://geoscope.ipgp.fr>.

**Table 2**  
*Geometric and Kinematic Parameters of the 30 October 2016 Earthquake as Proposed by Numerous Investigators*

Source	Length (km)	Width (km)	Min depth (km asl)	Strike (°)	Dip (°)	Strike (°)	Max slip m	Uniform slip m	$M_0$ (Nm)	$M_w$	Fault type	Method
Cheloni et al. (2017)	~20	-	0 <sup>a</sup>	~160	~40 <sup>b</sup>	-	>2	-	8.46e <sup>+18</sup>	6.59	Main rectangular fault	InSAR and GPS data inversion
	-	-	-	~160	-	-	~0.7-0.8	-	-	~6.1-6.2	Secondary rectangular fault	
	-	-	-	-	-	-	~0.7-0.8	-	-	~6.1-6.2	Secondary rectangular fault (either alternate or associated with the former secondary)	
Chiaraluce et al. (2017)	26	14	+0.850	151	47	~ -95	2.6	1.3	4.43e <sup>+18</sup>	6.4	One rectangular fault	Relocated earthquakes and strong motion data inversion
Liu et al. (2017)	32F	24F	0	155	46	-	3.1	-	10.5e <sup>+18</sup>	6.6	One rectangular fault	Strong motion and GPS data inversion
Papadopoulos et al. (2017)	17	-	0	158F	44F	-88F	1.4	-	6.6e <sup>+18</sup>	6.5	One rectangular fault	Modeling of seismological and InSAR data
Pavlidis et al. (2017)	25	15	0	152	44	-94	-	0.71	-	6.6	One rectangular fault	Geological observations; satellite imagery and InSAR data analysis
Pizzi et al. (2017)	-	-	X	160F	40F	-90F	~3	-	-	6.5	One rectangular fault	Strong motion data inversion
Scognamiglio et al. (2018)	34	16	+0.838	155	47	-90	2.8	0.4	5.9e <sup>+18</sup>	6.45	Main rectangular fault of two modeled faults	Seismological and geological observations (length/width/strike/dip/min depth); modeling of seismological and GPS data ( $M_0$ /average slip/Max slip)
Walters et al. (2018)	10	14	-0.950	210	36	~ -20	3.1	0.6	2.9e <sup>+18</sup>	6.25	Secondary rectangular fault of two modeled faults	
	12F	-	0	158F	40F	-135/-45F	n.r.	n.r.	n.r.	n.r.	Minor synthetic N	InSAR and GPS data inversion
	18F	-	0	155F	40F	-135/-45F	n.r.	n.r.	n.r.	n.r.	Vettore	InSAR and GPS data inversion
	8F	-	0	155F	40F	-135/-45F	n.r.	n.r.	n.r.	n.r.	Vettore	InSAR and GPS data inversion
	10F	-	0	165F	40F	-135/-45F	n.r.	n.r.	n.r.	n.r.	Vettore	InSAR and GPS data inversion
	15F	-	0	163F	45F	-135/-45F	n.r.	n.r.	n.r.	n.r.	Laga	InSAR and GPS data inversion
	10F	-	0	165F	40F	-135/-45F	n.r.	n.r.	n.r.	n.r.	Minor synthetic S	InSAR and GPS data inversion
	6F	-	0	325F	40F	-135/-45F	n.r.	n.r.	n.r.	n.r.	Minor antithetic	InSAR and GPS data inversion
	12F	-	0	340F	65F	-135/-45F	n.r.	n.r.	n.r.	n.r.	Norcia Antithetic	InSAR and GPS data inversion
	14F	-	0	222F	40F	-110/-20F	n.r.	n.r.	n.r.	n.r.	Pian Piccolo	InSAR and GPS data inversion
Wang et al. (2018)	40	-	-	128-175	33.5	-64.1	3.44	-	9.14 e <sup>+18</sup>	6.6	Variable-strike fault model	InSAR and GPS data inversion
Xu et al. (2017)	20	10	0°	160F	40	-99	-	1.3	7.85e <sup>+18</sup>	6.6	One rectangular fault- <i>uniform slip model</i>	InSAR and GPS data inversion
	30	18	0°	160	40	-89	2.5	0.55	8.97e <sup>+18</sup>	6.6	One rectangular fault- <i>distributed slip model</i>	

Note. F, fixed parameter; GPS, Global Positioning System; InSAR, interferometric synthetic aperture radar.

<sup>a</sup>Best fitting dip from GPS data = 40°; best fitting dip from differential interferometric synthetic aperture radar data = 37°. <sup>b</sup>This antithetic fault plane is illuminated by aftershocks that occurred soon after the 24 August earthquake.

(e.g., Bally et al., 1986; Barchi et al., 1998; Billi et al., 2006; Boccaletti et al., 1981; Calamita & Deiana, 1988; Cavinato et al., 1986; Cello et al., 1997; Di Luzio et al., 2009; Locardi, 1988; Patacca et al., 2008; Ricci Lucchi, 1986; Vai, 2001, among many others). The Apennines are an east verging, fold-and-thrust belt that developed during the Late Cretaceous-to-present Africa-Europe plate convergence (e.g., Alvarez et al., 1974; Dewey et al., 1989; Malinverno & Ryan, 1986, among others). The present-day landscape and tectonic setting of the region is the result of a long deformation history, characterized by cyclical extensional and contractional phases (for a summary see Vai, 2001).

The oldest deformation phase documented in the area is the Mesozoic rifting-drifting event and the subsequent evolution of the passive margin resulting from the opening of the Tethys Ocean (e.g., Bernoulli & Jenkyns, 1974). A major geodynamic change occurred in Cenozoic times when the closure of the eastern portion of the Tethys Ocean (Ligurian Ocean) marked the beginning of the Apennines' orogeny (Alvarez et al., 1974). During this time, the complex Mesozoic paleogeography was involved in the orogenic contraction and shortening, resulting in east verging thrusts and foredeep basins that progressively migrated from west to east (e.g., Barchi et al., 1998; Basili & Barba, 2007; Patacca & Scandone, 1989) toward the Adriatic foreland, in its turn simultaneously affected by extensional tectonics (e.g., Mazzoli et al., 2002).

### 2.1. Stratigraphic Setting

The nature of the deeper units and the basement underlying the Umbria-Marche Apennines remains rather obscure due to their absence in outcrops and to the lack of sufficiently deep wells. One may assume that the Hercynian basement is formed by metasedimentary and igneous rocks, as seen in the inner parts of the chain (e.g., in Tuscany: Bagnoli et al., 1979). Conversely, deep wells enabled the sampling of Carboniferous, Permian, and Middle-Lower Triassic rocks, which include slates, phyllites, red sandstones, and conglomerates (e.g., Anelli et al., 1994; Patacca et al., 2008), but the sparseness of the data makes it hard to reconstruct the thickness and lateral correlations of these rock bodies. More information is available for the overlying Triassic *Anidriti di Burano* Fm., composed of alternating anhydrite rocks, dolostones, and limestones (Martinis & Pieri, 1964; Figure 2). The Mesozoic rifting induced a substantial facies diversity, ranging from platform to basinal and pelagic limestones, marly limestones, and marls (from the *Calcare Massiccio* Fm. to the *Marne a Fucoidi* Fm.; e.g., Bernoulli & Jenkyns, 1974; Figure 2b). Hemipelagic cherty limestones and clayey marls deposited during the Oligocene and Miocene overlay such diverse units (from *Scaglia Cinerea* Fm. to *Marne a Cerrognola* Fm.; Bonarelli, 1899). In the central-eastern part of the Apennines (the Laga Basin), Messinian siliciclastic deposits dominate over the foothill area, and together with Pliocene sediments recorded the evolution of the foredeep basins and the associated Adriatic foreland (Selli, 1981; Figures 1 and 2).

### 2.2. Structural Setting

The oldest structures in the region are large extensional and transtensional faults of Jurassic-Eocene age. Some of them are clearly exposed, trend NW-SE, and are visibly truncated and passively conveyed in the hanging wall of the main thrust faults—the Mt. Sibillini thrust in our study area—through short-cut mechanisms (e.g., Mt. Petrella extensional faults; Calamita et al., 2011). Further faults are inferred only by stratigraphic relationships, such as thickness and facies variations across Mesozoic formations. The most representative of such inferred faults is indeed the NNE-SSW Ancona-Anzio lineament (Castellarin et al., 1978; Castellarin et al., 1982; Cavinato et al., 1986; Parotto & Praturlon, 1975), likely a regional paleogeographic feature that may have acted also as a lateral ramp or transpressional fault during the contractional phases (e.g., Calamita et al., 2012; Castellarin et al., 1978; Lavecchia, 1985; Tavarnelli et al., 2004).

The Neogene contractional history of the region has been accurately reconstructed using mesostructural observations. Most investigators agree that field data bear the evidence of different tectonic phases (Koopman, 1983; Lavecchia, 1985; Lavecchia et al., 1983; Tavarnelli, 1997). The first contractional phase is generally interpreted through a layer-parallel shortening mechanism, associated with extensive pressure-solution cleavage, followed by symmetric and asymmetric folding and terminated by a thrusting phase. Some investigators also highlighted extensional structures parallel to the hinge of the folds, possibly associated with the late thrusting phase (e.g., Barchi, 1991; Tavani et al., 2012). Despite a general agreement in the observation of mesostructures and their relative timing, differences exist in translating them into kinematic models. For instance, Lavecchia (1985) and Barchi (1991) suggest different and

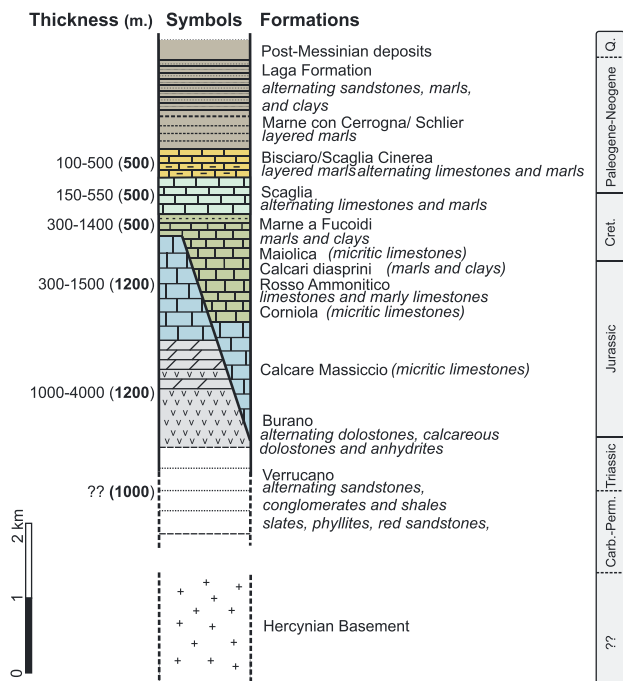


**Figure 2.** Stratigraphic column of the units cropping out in the central-northern Apennines (in color) and of the rocks that are presumed to occur at depth (modified from Scisciani, 2009). Figures in the left column represent the minimum and maximum thickness of each formation from the literature (see section 2.1); the bold figures in brackets indicate the estimate we used for our geological sections.

isolated tectonic phases, whereas Tavarnelli (1997) explains all structures with a single, progressive deformation mechanism.

Finally, the late-orogenic Quaternary extensional faults are well exposed in the western part of the chain, where they accompanied the development of intermountain basins (notably, the Tiber basin; e.g., Mirabella et al., 2011). Conversely, the recent extension is poorly expressed in the eastern zone (e.g., Ghisetti & Vezzani, 1997), thus making a direct association with seismogenic faulting at depth rather challenging (e.g., Bonini, Di Bucci, et al., 2014; Valensise & Pantosti, 2001; Vannoli et al., 2012).

### 3. The 2016–2017 Central Italy Earthquake Sequence

The 2016–2017 earthquake sequence occurred within a relatively narrow corridor running along the axis of the Apennines chain (see Figures 1 and 3a). Moment tensor solutions for the main events show nearly pure NE-SW extension (Figure 1). The 30 October mainshock revealed purely extensional kinematics along NNW-SSE striking planes, although its focal mechanism exhibits a large compensated linear vector dipole component (see Time Domain Moment Tensor solution in Table 1). The southwest dipping plane is compatible with the kinematics of many significant earthquakes that have occurred in the central and northern Apennines (e.g., Vannucci & Gasperini, 2004) and is consistent with the aftershock pattern (see Chiaraluce et al., 2017).

The surface displacement following this mainshock was accurately recorded through DInSAR techniques. Four interferometric image pairs are available in the literature, obtained with ALOS and Sentinel-1 satellites along ascending and descending orbits (see, for example, Figure S1 in Cheloni et al., 2017). Among these four data sets, the Sentinel-1 inter-

ferogram obtained from the ascending orbit (hereinafter S1-A) is the only publicly available data set that isolates the coseismic displacement field of the 30 October 2016 event.

Coseismic displacements have also been recorded by continuous GPS stations of the Istituto Nazionale di Geofisica e Vulcanologia-RING (Rete Integrata Nazionale GPS) network and by survey stations of the CaGeoNet (Central Apennine Geodetic Network) and IGM (Istituto Geografico Militare) networks; a combined solution of all these recordings has been assembled by the Istituto Nazionale di Geofisica e Vulcanologia Geodesy Working Group (2016) for both the Amatrice and Norcia events (Figure 3c).

Significant earthquake-induced surface effects were observed following the Amatrice earthquake. Ruptures, fractures, and landslides occurred over a large area, and in a more organized fashion along the upper western flank of the Mt. Vettore fault system for a total distance of about 5 km (Figure 3d; Emergeo Working Group, 2016; Martino et al., 2017). The Norcia mainshock caused a truly impressive system of surface ruptures; they in part overprinted those caused by the Amatrice earthquake, and in part modified the landscape further to the NW, overall affecting an area in excess of 400 km<sup>2</sup> (Civico et al., 2018; Villani et al., 2018; Figure 3d).

## 4. Geodetic Constraints on Earthquake Source Geometry

To propose a model for the seismogenic source of the Norcia earthquake, we first used the coseismic displacements detected by GPS and DInSAR to obtain the basic fault parameters, such as fault dip, and to test different solutions with fault geometries inferred from aftershock patterns and focal mechanisms.

### 4.1. Determining the Dip of the Seismogenic Source

To define the average dip of the seismogenic source, we first built an inversion procedure aimed at generating a suite of models for a range of dip angles, then we analyzed the resulting model residuals. The analysis of the dip angles in our inversion scheme is not purely linear, since we compute a separate linear inversion for each dip angle, introducing the nonlinear dependence of the deformation field from the dip angle. We

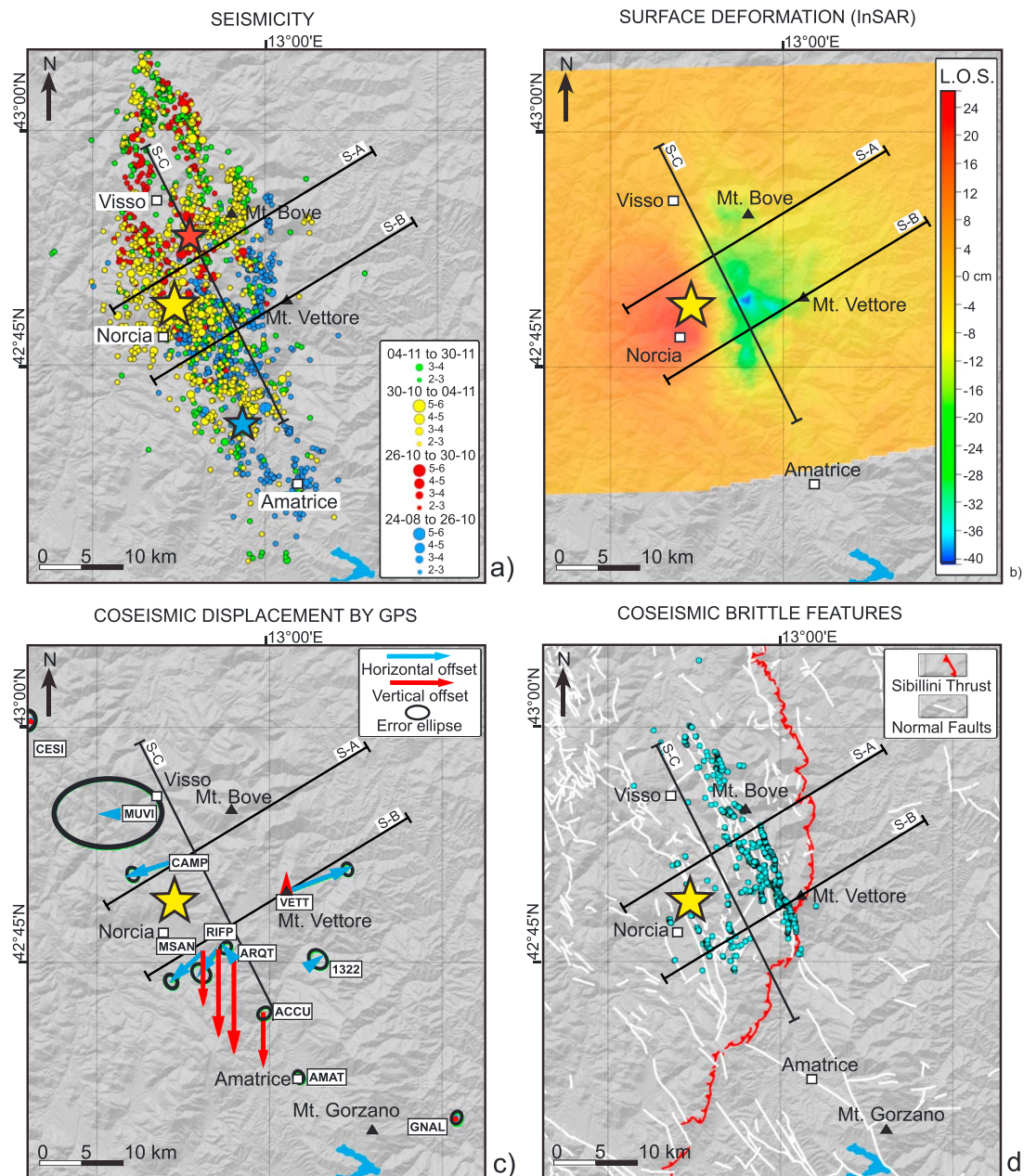


**Figure 3.** (a) Mainshocks and aftershocks of the whole sequence (color-coded by time ranges). (b) Map view of the displacement field (line of sight, interpolated) over the Amatrice-Norcia area detected by S1-A (Bignami, 2017). (c) Coseismic Global Positioning System (GPS) displacements (both horizontal and vertical, with error ellipses where available) as recorded by Istituto Nazionale di Geofisica e Vulcanologia (INGV) permanent and temporary stations. (d) Coseismic features recognized in the field following the 24 August and 30 October mainshocks. The main features, here represented with a single symbol (light cyan dots) for ease of reading, include bedrock ribbons, fractures, dislocations, ruptures with offset, liquefaction, and landslides (data from Civico et al., 2018; Villani et al., 2018). In all four panels, a yellow star marks the epicenter of the Norcia earthquake, whereas the black segments show the traces of the cross sections in Figures 5, 10, and 11.

obtained the deformation field from two S1-A images, acquired by Sentinel-1A on 27 October 2016 and 2 November 2016, respectively, with 20-m spatial resolution and an average incidence angle of  $32.2^\circ$  along the ascending orbit (Bignami, 2017). This short temporal baseline ensures that the contribution of any preseismic and postseismic deformation is minimized.

S1-A includes about 5,500,000 single measurement points and must hence be decimated before its use in a numerical inversion procedure. To this end, we first cropped the original frame to discard far-field areas

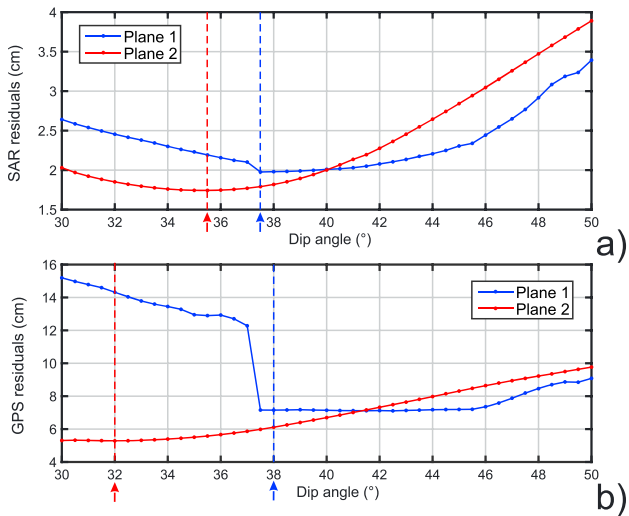


**Figure 4.** Root-Mean-Square of residuals as a function of dip angle for two rectangular planar sources (Plane 1 and Plane 2: see text). (a and b) The root-mean-square of residuals for the differential interferometric synthetic aperture radar (DInSAR) and Global Positioning System (GPS) data sets, respectively. The arrows indicate the best fitting dip for either plane.

where coseismic deformation is close to null, then reduced the data set to about 13,000 single measurements with a pixel size of about 400 m (Figure 3b). S1-A shows significant offsets over an area of about  $40 \times 40 \text{ km}^2$ . Extreme changes along the satellite line of sight (LOS) are  $-40.8$  and  $+26.3$  cm, respectively. Overall, the data show a central area of negative LOS offsets surrounded by two lobes of positive LOS offsets to the ENE and WSW (Figure 3b). It is important to stress that the incidence angle of S1-A and the geometry of the earthquake causative fault(s) combine in such a way that the component of horizontal ground displacement along the LOS is substantial, implying that the deformation field in Figure 3b is by no means representative of coseismic uplift/subsidence alone.

DInSAR data are complemented by data from 14 continuous GPS stations falling within the region covered by S1-A (see Figure 3c). GPS offsets confirm the marked subsidence of the hanging wall, with the largest subsidence of 44.7 cm recorded at ARQT. Horizontal offsets, the largest being observed at VETT (38.3 cm eastward), indicate extension along a WSW-ENE axis. We tested the consistency of the SAR and GPS data sets by projecting the three-dimensional coseismic GPS offsets on the S1-A LOS direction and comparing them with data from the DInSAR field. The results indicate a generally good agreement with no systematic misfits (Figure S1).

In all our geodetic models the rupture planes have been discretized into  $1 \times 1 \text{ km}$  uniform-slip patches. For each patch, we computed the expected offset at the GPS sites and at the location of each DInSAR pixel assuming unitary slip in both the strike-slip and dip-slip directions, using Okada’s (1992) analytical solutions. These unitary deformation fields are used to build a Green’s function matrix  $G$  through which the expected deformation field can be obtained as  $\mathbf{d} = G \mathbf{m}$ , where  $\mathbf{d}$  and  $\mathbf{m}$  are vectors containing deformation data and slip values at each patch, respectively. The estimate of the model vector  $\mathbf{m}$  is then obtained by inverting the  $G$  matrix in the least squares sense. In the inversion process we introduced a positivity constraint to limit rake angles between  $-45^\circ$  and  $-135^\circ$ , following the accelerated version of the Lawson and Hanson (1974) scheme proposed by Van Benthem and Keenan (2004). In order to avoid large, physically unrealistic heterogeneities of the slip distribution on the fault plane, we minimized a discrete approximation of the 2-D Laplacian operator along with the data-model residuals. The relative weight of the smoothing term with respect to the data term was calibrated by computing a range of linear inversions with a varying weighting factor, setting the weight at the knee of the corresponding roughness-misfit trade-off curve (Figure S2). We included in the inversion scheme an additional relative weight between the GPS and DInSAR data sets: this weight was fine-tuned in order to balance the misfits between the two data sets.

In this first stage, we assumed that the rupture occurred over a  $25 \times 20 \text{ km}^2$  rectangular plane striking  $156^\circ$ , the average of all strike angles derived from focal mechanisms (Table 1). We applied the procedure previously described in two different ways. As a first option, we assumed that the rectangular fault crosses the hypocenter and reaches the surface with its upper edge. This model is referred to as *Plane 1*. Since the medium in our modeling is a simple half-space that does not include topography, we adjusted the hypocentral depth to account for the average local topography. As a second option, we adopted a plane whose upper tip is located below the reported surface breaks and varied its dip angle, thus relaxing the requirement that the plane must cross the hypocenter. This model is referred to as *Plane 2*.

#### 4.1.1. Dip of the Main Fault at Depth

For both options, we calculated the best fitting dip angle separately from DInSAR and GPS data (Figure 4).

The best fitting dip obtained for Plane 1 from both the DInSAR and GPS data sets is  $\approx 38^\circ$ . For Plane 2 the best fitting dip is  $\approx 36^\circ$  and  $\approx 32^\circ$ , respectively, from DInSAR and GPS data: they are both lower than the best fitting dip obtained for Plane 1. For a dip  $< 38^\circ$  the RMS increases sharply for GPS data and more gently for DInSAR data. As for GPS residuals, the sharp increase is due to the VETT station, whose position switches from the fault footwall to the fault hanging wall, resulting in the model being unable to reproduce its large



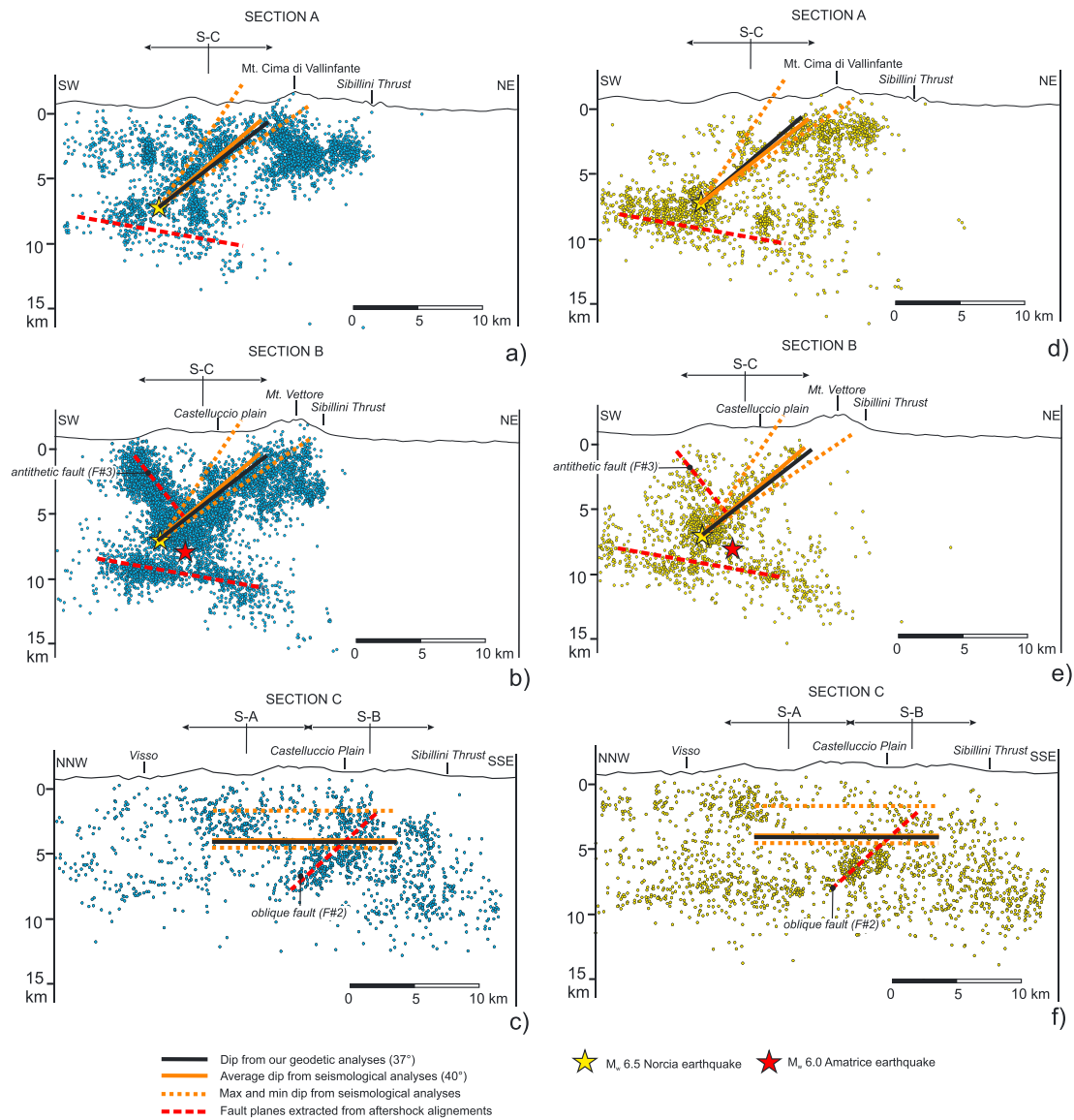


**Figure 5.** Profiles showing aftershock distributions (data from Chiaraluce et al., 2017) falling within a 2.5-km range from the section plane (see Figure 3 for the location of the sections). The blue and yellow dots indicate earthquakes recorded before and after the 30 October event, respectively. The thick black lines represent the main seismogenic source obtained from our geodetic analyses. The thick orange lines represent the average dip obtained by various studies (Table 1). The dashed red lines are faults inferred from aftershock alignments.

eastward offset. The presence of a ramp around the same dip value also in the DInSAR residuals constrains rather strongly the location of the updip projection of the seismogenic fault plane.

Since in the rest of our analysis we deal with constant-dip planes, we chose to adopt the average of the two best fitting values from DInSAR data ( $37^\circ$ ).

#### 4.2. 3-D Seismogenic Models

In this stage we test different fault configurations with joint linear inversions of DInSAR (S1-A data set) and GPS data. The best fitting model predictions and the corresponding residuals will be used to check the goodness of fit for different fault configurations.

Figure 5 shows the aftershock distribution before and after the Norcia earthquake along three 2-D sections: two perpendicular and one parallel to the main fault. Deriving the geometry of a seismogenic fault from an

**Table 3**  
Main Parameters of Modeled Faults

Modeled faults	Strike (°)	Dip (°)	Min. rake (°)	Max rake (°)	X (m)	Y (m)	Length (km)	Bottom depth (km)
F#1	156	37	-135	-45	351,701	4,745,135	26.7	8.4
F#1b	156	37	-135	-45	350,074	4,748,789	19.1	8.4
F#2	206	49	-135	-45	351,472	4,734,978	20.0	8.4
F#3	335	58	-135	-45	349,420	4,741,005	17.5	3.4

Note. X and Y (UTM33N, WGS84, and EPSG: 32633) refer to the center of the surface trace of the model fault.

aftershock distribution is inherently ambiguous because it is difficult to separate on-fault and off-fault seismicity; besides, the main slip patches are generally devoid of aftershocks and are hence *invisible* to this type of analysis. In our case, these circumstances may have been amplified by the occurrence of two large earthquakes and the associated aftershocks along adjoining faults, not to mention the possible occurrence of foreshocks of the Norcia earthquake. For the main fault, these limitations can be overcome using the mainshock hypocenter and our previous estimate of fault dip (see section 4.1), fixing fault strike as the average obtained from focal mechanisms (156°).

Inferring the parameters of additional faults is far more difficult and highly subjective. An alignment of aftershocks seen in both cross sections suggests the existence of a rather deep, low-angle, east dipping plane (Figure 5), activated soon after the Amatrice earthquake. In section view, especially in Section B, an aftershock alignment depicts a high-angle east dipping fault. The temporal evolution of the aftershocks suggests that this antithetic structure was activated soon after the Amatrice mainshock and that only minor shocks fell along it after the Norcia mainshock. In Section C, that runs along-strike, a prominent aftershock cloud suggests the activation of an oblique fault with a NE-SW strike.

In summary, the joint analysis of aftershock distributions, seismological evidence from the mainshocks, and geodetic offsets allowed us to identify three principal faults: a main fault coinciding with the hypocenter (Fault#1), an oblique northwest-dipping fault (Fault#2), and a northeast-dipping fault, antithetic to the main fault (Fault#3). A further very low-angle fault lies at the base of the investigated crustal volume. These findings on the main faults activated at depth agree with the results proposed by the majority of other studies on this sequence (e.g., Chiaraluca et al., 2017; Scognamiglio et al., 2018; Walters et al., 2018). Significant discrepancies may exist only in the discrimination of their role during the three mainshocks and during the early postseismic phases.

As mentioned earlier, scrutiny based exclusively on aftershock locations can be highly speculative. To prevent the consequences of making a wrong initial assumption on the timing of activation of these faults, we modeled different fault configurations. In a first model, we used only the main fault (Fault #1), whose plane crosses the hypocenter, strikes according to the average of seismological determinations (~156°; Table 1), and dips 37°, our best fitting angle calculated in the previous stage (Table 3). In a second model we added Fault#2, which strikes at an angle with the main trend; based on the aftershock pattern we set its strike and dip at 206 and 49°, respectively. In a third model, we added the antithetic Fault#3; its strike and dip were set at 335 and 58°, respectively (Table 3), based again on the aftershock pattern. In all three models, the southern end of Fault#1 is not bound by the oblique Fault#2. To test what would happen if this were the case, that is, if Fault#1 terminates against Fault#2, we set up two additional models where the main fault is truncated at its southern end (Fault #1b). Also, for this second set of models we first added only the oblique Fault#2, then the antithetic Fault#3. In all models, the fault planes were discretized into  $1 \times 1 \text{ km}^2$  patches and embedded in a uniform half-space.

#### 4.2.1. Results

The resulting slip distribution for the unconfined single-plane fault (Figure 6a) exhibits a well-defined high-slip patch located in the southernmost portion of the plane, which is about  $4 \times 4 \text{ km}^2$  in size and falls in the deepest portion of the plane at 5- to 7-km depth. The average rake angle of the main slip patch is  $-135^\circ$ . Assuming a crustal rigidity of 26 GPa, the resulting seismic moment is  $M_0 8.78 \cdot 10^{18} \text{ Nm}$ , corresponding to a geodetically-derived  $M_w 6.59$  (for a crustal rigidity of 33 GPa, we obtain  $M_w 6.65$ ). Slip directions within the high-slip patch exhibit a nonnegligible right-lateral component.

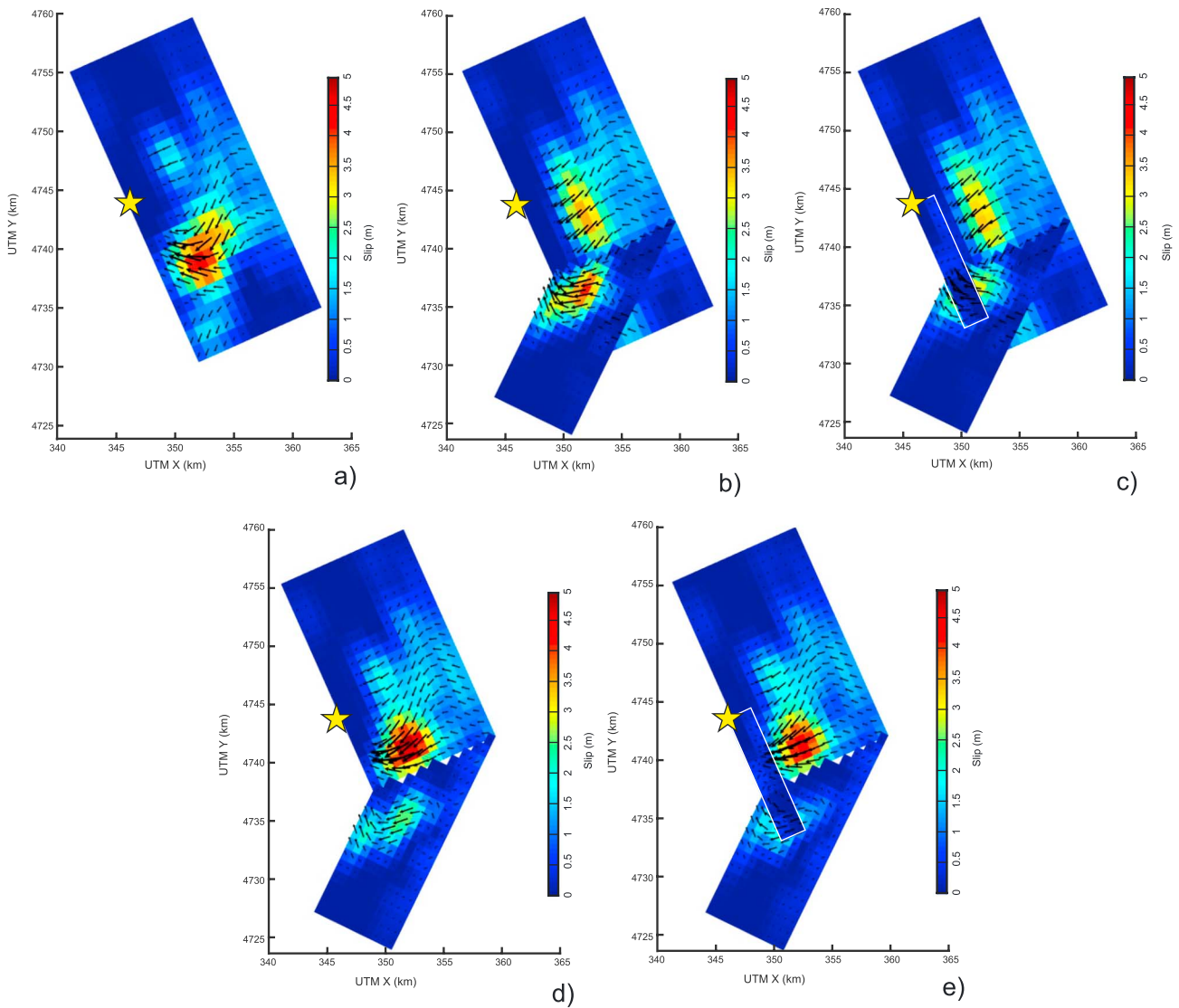


**Figure 6.** Slip distribution resulting from the least squares linear inversion of interferometric synthetic aperture radar (InSAR) data for all fault configurations: (a) from a single and unconfined fault (Fault#1); (b) with an additional oblique fault (Fault#2) or (c) two additional faults, one oblique and one antithetic (Fault#2 and Fault#3); (d) with a confining oblique fault (Fault#2); or (e) two additional faults, one confining oblique and one antithetic (Fault#2 and Fault#3). The color coding represents absolute slip values; the arrows show the surface projection of the rake direction. A yellow star marks the epicenter of the 30 October 2016, Norcia mainshock.

The slip distribution changes significantly after adding the oblique Fault#2 to the model (Figure 6b). It shows two main slip patches, one of which is located on the oblique fault and is rather prominent. The rake angles are close to  $-90^\circ$  for Fault#1 and  $-45^\circ$  for Fault#2. Minor slip is seen in the hanging wall of Fault#2.

The location of the two main slip patches is not significantly affected by the introduction of the antithetic Fault#3 (Figure 6c); nevertheless, slip on Fault#1 decreases slightly as a consequence of the slip mapped onto the new fault. The rake of the slipped patch on Fault#1 is close to  $-90^\circ$ , as in the previous model, but it rotates up to  $-90^\circ$  in the upper part of the slipped patch in Fault#2. Even in this case, some slip is mapped in the southernmost portion of Fault#1, that is, in the footwall of the oblique fault.

In the last two models, that were designed such that Fault#1 terminates at the intersection with oblique Fault#2 (Figures 6d and 6e), the main slip patch lies on Fault#1 and exhibits a rake angle close to  $-90^\circ$ .

**Table 4**  
*Weighted Root-Mean-Square of Residuals (WRMS), Normalized Chi Squared, and Geodetic Magnitude for All the Explored Models*

Modeled faults	WRMS (cm)			Chi squared/DOF	$M_w$
	Global	SAR	GPS		
F#1	3.75	1.92	4.63	4.82	6.58
F#1, F#2	2.43	1.72	2.83	2.16	6.63
F#1, F#2, F#3	1.91	1.64	2.08	1.35	6.62
F#1b, F#2	2.98	1.76	3.61	3.26	6.60
F#1b, F#2, F#3	2.20	1.72	2.49	1.80	6.58

Note. DOF, degree of freedom.

In the model with no antithetic fault the rake is close to  $-90^\circ$  in the main slip patch on Fault#1 and close to  $-45^\circ$  in Fault#2. Also, in this case, the antithetic Fault#3 has a limited effect on the slip distribution and the rake of oblique Fault#2.

The RMS of residuals for the best fitting solutions is quite low and is even lower for the multiple-fault models, as largely expected (Table 4). The comparison between the observed and predicted DInSAR displacement fields for all fault configurations is shown in Figure 7. We remark that all of them reproduce the main features of the observed field without any evident systematic misfit, implying that the contribution from Fault#1 largely dominates over that from Fault#2 and Fault#3.

Figure 8 compares observed and predicted coseismic offsets at the 14 considered GPS stations. Horizontal and vertical offsets are rather well reproduced by the all models at all sites, but the single model fault inevitably exhibits larger misfits. In particular, all models reproduce well the horizontal offset at VETT; this offset is controlled by the surface projection of the main fault, which is the same for all geometries. Significant horizontal offsets at sites on the hanging wall are generally better reproduced by the multiple-plane geometries, with the sole exception of ARQT, that fall near the junction of Fault#1 and Fault#2 and may hence be affected by model artifacts or may be sensitive to small-scale details.

## 5. Geological Modeling of the Epicentral Area

### 5.1. Available Data

To reconstruct the large-scale architecture of the subsurface in the epicentral region, we first revised all the available information. All data were initially separated into *surface* and *subsurface*.

With regard to surface data, numerous geological maps have been published, describing in detail the stratigraphy and structural arrangement of the outcropping formations of the Amatrice-Norcia area (e.g., Bigi et al., 1992; Boncio et al., 2009; Centamore et al., 1992; Centamore & Rossi, 2009; Cello et al., 1997; Giunta Regione Marche, 2014; Mazzoli et al., 2005; Pierantoni et al., 2013; Servizio Geologico d'Italia, 1941, 1952, 1955, 1958, 1963, 1965, 1966, 1967, 1968a, 1968ab, 1969, 1970; Vezzani & Ghisetti, 1998; Vezzani et al., 2010).

Available subsurface data comprise different types of observations and some deductions from geophysical studies. The observations include seismic reflection data acquired during oil and gas exploration. More specifically, there exist three seismic profiles crossing the epicentral area of the Norcia earthquake and various profiles in the footwall of the Sibillini thrust (see Figure 3 in Porreca et al., 2018). A seismic profile crossing the southern area has been recently interpreted by Porreca et al. (2018); another profile crosses the area from south to north but is not publicly available. A further profile running roughly E-W was published for the first time in Bally et al. (1986).

In general, seismic reflection data illuminating the hanging wall of the Sibillini thrust are characterized by scattered reflectivity and by a relatively poor resolution (Porreca et al., 2018). Along with the lack of deep wells, these circumstances significantly increase the uncertainties in the interpretation of the subsurface architecture, thus representing a typical case of subjective uncertainties, where multiple, equally valid interpretations can be proposed.

Conversely, the quality of seismic profiles allows the structures in the footwall of the Sibillini thrust to be imaged quite well (Figure 1). For instance, different investigators agree in describing a well-developed thrust-related fold, the Acquasanta Anticline (e.g., Porreca et al., 2018; Scisciani, 2009). As the uncertainties on the geometry of this structure are small, we used it as a constraint in the subsequent modeling steps.

As for the geophysical studies, Chiarabba et al. (2018) recently published a seismic tomography model for the area, having a horizontal and vertical resolution of 5 and 3 km, respectively. The model shows that in the area of the Norcia earthquake the inferred  $P$  wave velocity falls in the range 6.0–6.5 km/s, all the way from 3- to 15-km depth, without significant fluctuations. This  $V_p$  value characterizes most formations in the area

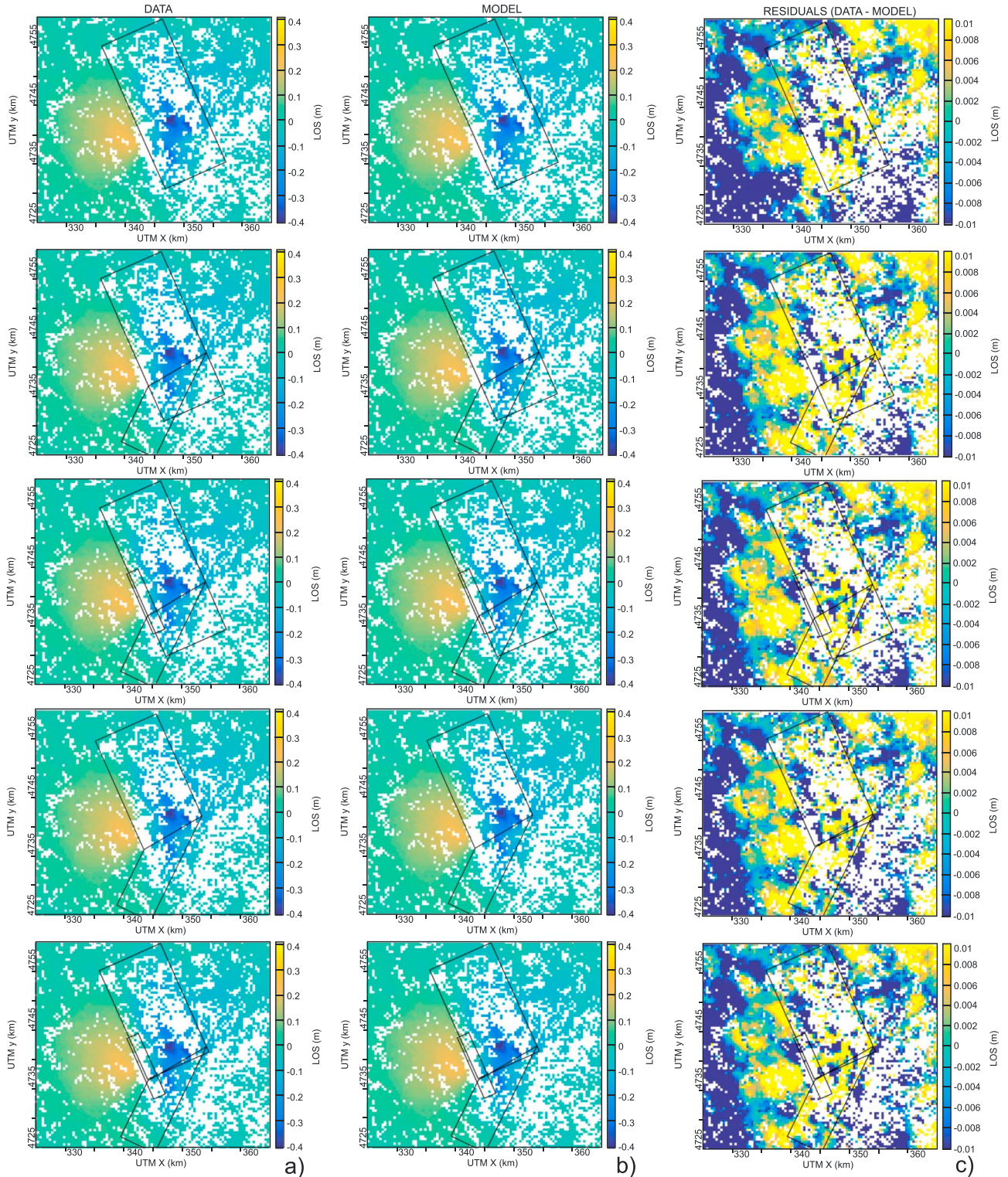


**Figure 7.** Best fitting coseismic displacement fields imaged by differential interferometric synthetic aperture radar (DInSAR) interferometry for different fault configurations (see Figure 6 and section 4.2). The left-hand panels (a) show the observed LOS offsets; the central panels (b) show their best fitting model predictions, and the right-hand panels (c) show the corresponding residuals (data minus model). Notice that the color scale of the (a) and (b) panels is not the same as that of the (c) panels. Also recall that the incidence angle of the Sentinel-1 sensor implies that LOS changes contain a substantial component of horizontal offset, such that the retrieved deformation field is by no means representative of coseismic uplift/subsidence alone.

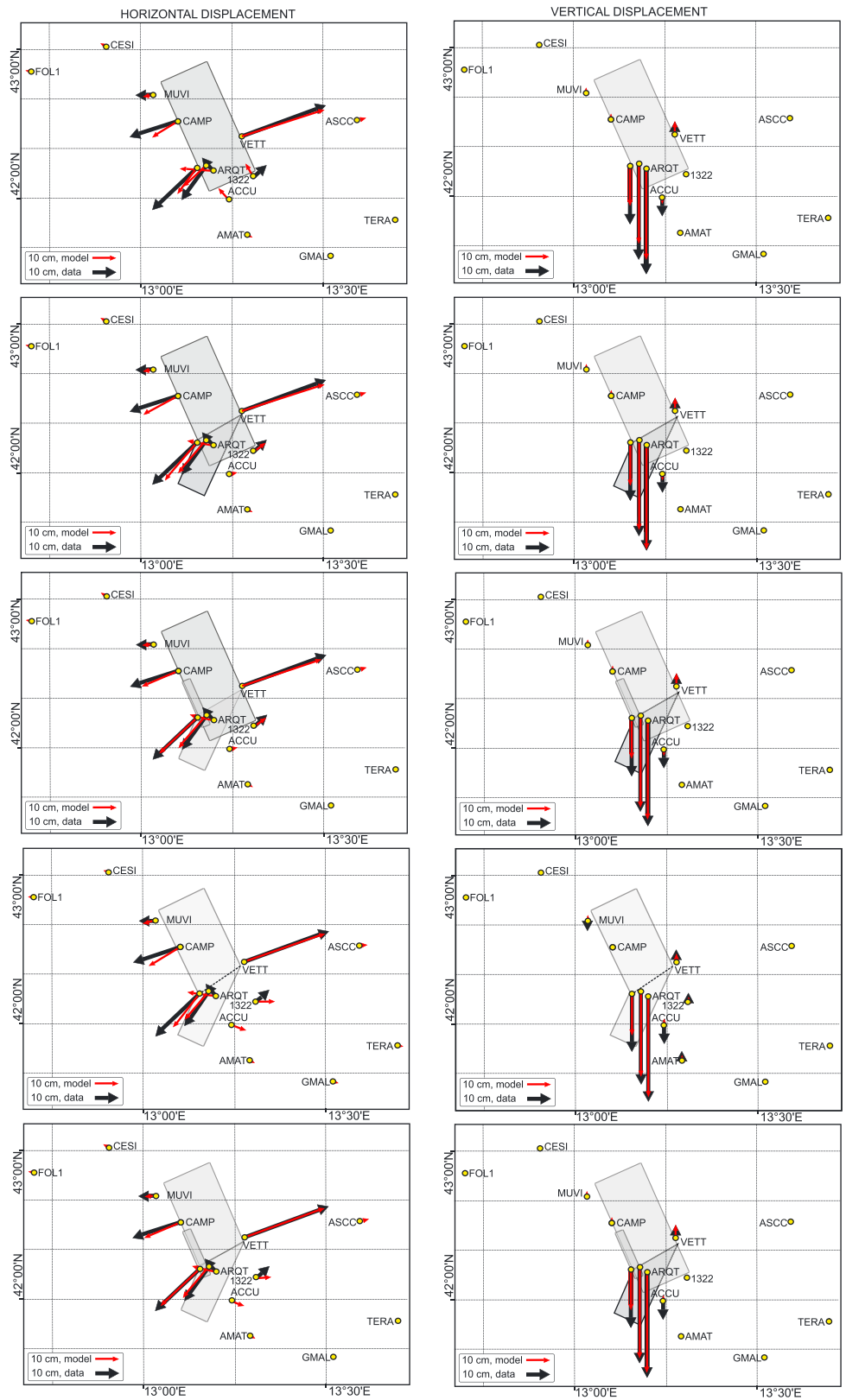


**Figure 8.** Coseismic offsets calculated at the considered Global Positioning System (GPS) stations and corresponding predictions from the best fitting slip patterns for all fault configurations (same as in Figure 7). The black and red arrows show observed and modeled offsets, respectively. The shaded gray boxes represent the surface projection of each fault plane.

(e.g., Porreca et al., 2018; Scisciani, 2009), except for the Cretaceous to Quaternary formations and some facies of Permo-Triassic rocks. Hence, this model could not be used to constrain the geometry of the different formations at depth, but it allowed us to rule out the presence of thick low-velocity layers in the upper crust.

## 5.2. Modeling Procedures

From the analyses of available data and considering the inherent uncertainties in the interpretation of subsurface data, we decided to adopt multiple working hypotheses (in the sense of Chamberlin, 1965). To reduce the number of possible solutions, we must first make some assumptions stemming from the geology of the shallower portion of the crust.

We used published maps to create a synthetic geological map of the epicentral area of the Norcia earthquake. We reconstructed the structures of the shallower crust along the same three profiles we used to analyze the aftershock distribution (Figure 5). Considering the epistemic uncertainties involved in any geologic interpretation, we limited the maximum depth of the interpretation along these sections to the bottom of the Jurassic *Calcare Massiccio* Fm., the oldest formation cropping out in the region. Our sections thus show only the shallower portion of the crust, down to about 4-km depth, including the necessary geometrical simplifications due to scale-of-display and cross-scale adaptations.

These shallow sections formed the basis for the ensuing interpretation of the deeper portions of the upper crust, aided by the subsurface architecture derived from seismic reflection data from the footwall of the Sibillini Thrust. Based on these constraints, we created multiple interpretative solutions for the seismogenic volume extending from 3- to 4- to 10-km depth. We aimed to build tectonic models spanning the full range of solutions arising from the known data and the associated uncertainties.

The main source of uncertainty concerns the tectonic style used to guide the reconstruction of the contractional phase that is responsible to the present tectonic setting. As the choice of a thin- or thick-skinned model is still a live issue in the central Apennines (e.g., Scisciani et al., 2014; Tavarnelli et al., 2004), we decided to follow both alternatives.

The second major source of uncertainty is the unknown location of the main décollement levels, especially in thin-skinned models. Barchi (1991) already showed that the depth of this décollement significantly affects the architecture of the subsurface. There exists a good agreement on the depth of the upper, main décollement level found along the stratigraphic succession of the Umbria-Marche Apennines (e.g., Barchi, 1991) that lies at the top of Meso-Cenozoic carbonate sequence (i.e., at the top of the *Scaglia Cinerea* Fm.). In contrast, different investigators locate the main lower décollement at widely different stratigraphic levels; for example, at the bottom of the Triassic evaporites (*Anidriti di Burano* Fm.) or in the weak Permo-Triassic continental deposits (e.g., Mirabella et al., 2008).

We created two models based on a thin-skinned tectonic style; in recognition of the above limitations, however, the lower décollement level is located either along the Triassic evaporites of the *Anidriti di Burano* Fm. (Tectonic Model#1) or at the base of Permo-Triassic deposits (Tectonic Model#2). Our third model (Tectonic Model#3) is based on a thick-skinned style; hence, its main structures do not root along large décollements but presumably coincide with precontractional normal faults.

Given that we lack detailed direct information on the thickness of formations that do not crop out in the area, we assigned constant thickness to all units, knowing that any departure from this simple assumption would be arbitrary. For the same reason, we did not introduce any precontraction faults, except in those areas and models where a limited orogenic shortening allowed the introduction of the abandoned roots of shortcut extensional faults.

In all three models the postorogenic extensional faults, or the thrust faults reactivated as normal by negative inversion, exhibit geometrical parameters that are similar to those obtained from aftershock distributions, from focal mechanisms, and our geodetic study. As we are aware of the epistemic uncertainties involved in both seismological and geodetic analyses, we adapted the postorogenic architectures to the three different tectonic scenarios. To avoid or limit a cognitive bias, this adaptation, as well as the choice of the geometry and kinematics of the orogenic structures, must follow prespecified rules.

Several alternative approaches may be used to analyze and quantitatively predict the geometry of the structures at depth; these include (a) balancing cross sections, (b) making assumptions based on

kinematic models, and (c) resorting to rock mechanics. These approaches are needed to answer two fundamental questions: (1) what is the geometry of the structure? And (2) what process (es) determined such geometry? (Fletcher & Pollard, 1999). Geometrical analyses play a fundamental role in answering the first question; for instance, the construction of balanced and restorable sections allows for predicting and testing the geometry of the structures at depth, especially in zones for which no direct data exist (e.g., Dahlstrom, 1969; Groshong et al., 2012). The trace of the cross sections that we used to define our three tectonic models was drawn nearly perpendicular and parallel to the strike of the activated faults, but they are not perpendicular to the trend of the Sibillini Thrust as they fall close to the lateral ramp of this regional structure. Hence, out-of-plane strain makes it difficult to balance and restore our 2-D models from a purely geometrical point of view, and a full 3D model is still unavailable. Nevertheless, we can constrain our models from a mechanical point of view, selecting the best geometry and kinematics of the structures in relation to the mechanical stratigraphy. As the mechanical stratigraphy strongly controls the geometry and kinematics of the faults and related folds, both for contractional and extensional structures (e.g., Brandes & Tanner, 2014; Ferril et al., 2017), we built our three tectonic models coherently with the mechanical features of the faulted rocks and with the appropriate relationships between faults and folds.

One of the fundamental steps that may help to select the correct geometrical or kinematic model is to pick the appropriate propagation-to-slip ratio or displacement-to-fault length relationship in relation to the type of rocks and the mechanical features of the given rock sequence. In nature, faults in competent rocks nucleate and propagate much faster than they do in incompetent rocks. This observation implies that in a volume of competent rocks, shortening or extension is more likely to be accommodated by faulting rather than by folding (brittle vs. ductile deformation). Therefore, to solve a relationship between a fold and a fault, the modeler must select a kinematic model in which the propagation-to-slip ratio is very high, and the displacement along the fault plane is close to constant. A correct choice for this example is the fault-bend-fold model, where the displacement along a fault ramp is assumed constant. Conversely, if a propagation-to-slip ratio is thought to be low due to the mechanical characteristics of the given rock sequence, the selected kinematic model should be a fault-propagation fold, where the displacement along the fault plane is not constant.

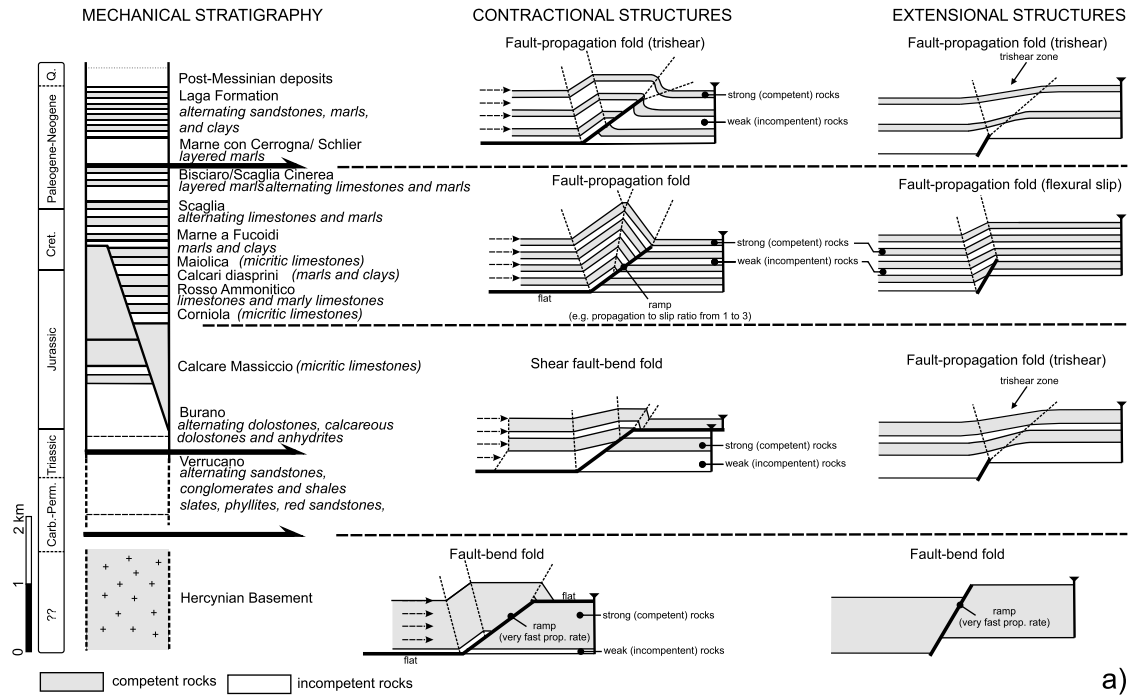
The Umbria-Marche stratigraphic sequence is mechanically heterogeneous, as competent units (e.g., Jurassic limestones; *Calcare Massiccio* Fm.) typically alternate with weaker ones (e.g., Triassic evaporites; *Anidriti di Burano* Fm.). To reconstruct subsurface structures, we must first assume a kinematic model (Figure 9). As the faults cut through different formations, a different kinematic model may have to be adopted depending on the location of the propagating tip. More specifically:

1. The basement rocks are mainly composed of competent units such as igneous rocks (see section 2.1), and consequently, faults grow with a very fast propagation-to-slip ratio. In this case, our preferred kinematic model is the fold-bend fault.
2. The Carboniferous and Permo-Triassic rocks are relatively incompetent and are overlain by competent Triassic and Jurassic rocks. In this case, we adopted the shear-fold-bend faulting model that predicts distributed shear in weak rocks and early fault inception in competent rocks. Such model implies, for example, that the maximum displacement will not occur close to the flat-ramp transition of a thrust system, but in the region where fault ramp cuts competent rocks (e.g., Hughes & Shaw, 2014).
3. The Cretaceous to Lower Paleogene sedimentary sequence (from *Corniola* to *Scaglia Cinerea* Fms.) is characterized by alternating limestones, marls, and clays. In such rock types, the cyclical transition between strong and weak layers suggests that the kinematic model to be preferred is the kink-band fold-propagation fault for reverse faults (Bonanno et al., 2017; Hughes & Shaw, 2015) and a flexural slip model for the extensional structures.
4. All younger formations, from Paleogene to Quaternary, are dominated by weak rocks. In this case, our preferred model is trishear fault-propagation fold.

Dealing with mechanical stratigraphy implies also anticipating the effects of the mechanical boundaries that are known to exist in a rock sequence. A proper modeling procedure must consider the effect of all existing low frictional surfaces—which include faults and stratigraphic discontinuities—on the evolution of both contractional and extensional structures (Figure 9). If a weak layer located above a propagating fault

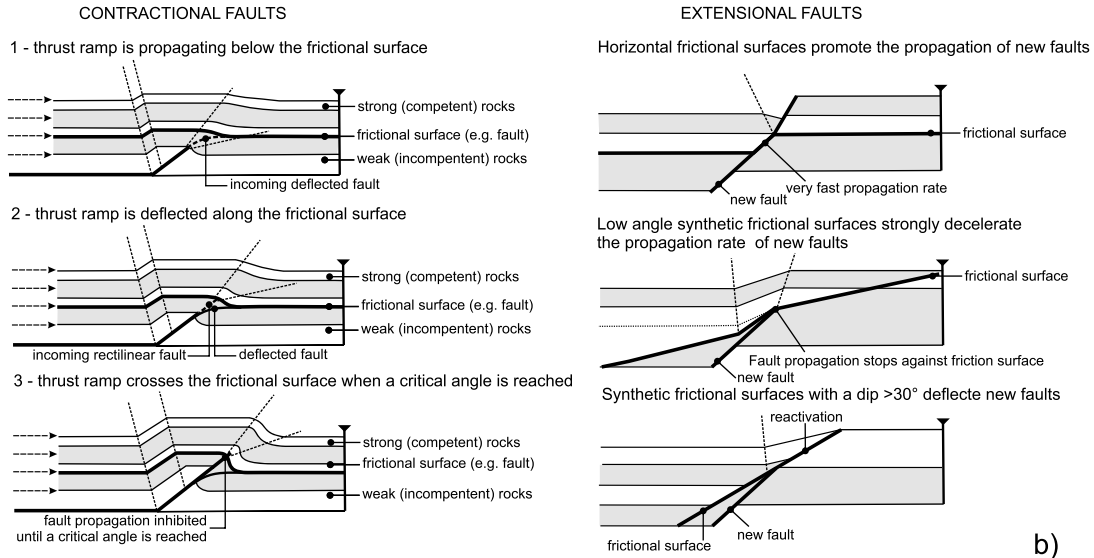


## EFFECTS OF STRATIGRAPHY ON STRUCTURAL STYLES



a)

## EFFECTS OF EXISTING FRICTIONAL SURFACES ON THE PROPAGATION OF NEW FAULTS



b)

**Figure 9.** (a) On the left we show the local stratigraphic column with the main décollement levels marked by thick, black arrows. On the right, we show the kinematic models selected to reconstruct fault-fold relationships at each stratigraphic level. (b) Summary of the effects that thin frictional discontinuities may have on the propagation of new faults.

causes its plane to be refracted (i.e., steepening for extensional faults and shallowing for reverse faults) and its characteristic propagation-to-slip ratio to be delayed, the role of a frictional weakness becomes more complex. Several investigators have explored this effect using analog and numerical models (e.g., Albertz & Sanz, 2012; Bonini et al., 2015; Bonini, Basili, et al., 2016; Bonanno et al., 2017; Hughes & Shaw, 2015; Roering et al., 1997).

In the case of a reverse fault (e.g., a thrust ramp), a frictional surface located ahead of the propagating tip initially deflects the fault plane along the frictional interface, mimicking a ramp-flat geometry (e.g., Bonanno et al., 2017). As stress increases, a new fault splay forms and become able to cross the frictional discontinuity when the angle between the two structures reaches a critical value (Bonanno et al., 2017). Note that until the critical angle is not reached, the propagating fault merely is stopped below the frictional surface (Figure 9b). This effect is proportional to the friction coefficient of the discontinuity: the lower the friction, the larger the halting effect (Bonanno, 2018).

For extensional faults, knowing that the frictional properties of the weak surface are critical, also, the relative orientation of the new and the existing structures plays a significant role (Bonini et al., 2015). For instance, a horizontal frictional surface ahead of the propagating tip of an extensional fault increases the propagation rate of new faults. Conversely, if the existing frictional surfaces are low-angle and dip opposite to the propagating fault, the propagation rate may be two times slower than in the previous case (Bonini, Di Bucci, et al., 2014). When the dip of existing frictional surfaces is  $\geq 30^\circ$ , these surfaces can be reused as extensional faults. As a result, all these different interactions also impact the magnitude of the fold-related extensional faults (Bonini et al., 2015). Since our tectonic models are designed at a regional scale, we use these rules only for major frictional surfaces that coincide with existing faults, either contractional or extensional. The effects of minor frictional surfaces (e.g., flexural slip along interlayer surfaces) are considered in the choice of kinematic models.

### 5.3. Modeling Results

#### 5.3.1. Geological Map and Shallow Sections

The first step of our modeling procedure is to draw a geological map summarizing data from a variety of sources (Figure 10). Since the scale of our analyses is large, we necessarily simplified some stratigraphic and structural features, for instance, by grouping various formations together or omitting small faults. The resulting map shows that Mesozoic carbonates dominate the area western half, post-Messinian foredeep deposits dominate the eastern half, and the regional Sibillini thrust separates these two halves. Several extensional faults occur both in the footwall and in the hanging wall of this regional structure. These faults were generated during preorogenic, synorogenic, and postorogenic phases, although assigning each of them to the relevant stage is not straightforward. Some faults occurring in the hanging wall are positively preorogenic, as they die out against exposed thrust planes due to a short-cut mechanism (e.g., Monte Petrella area; Scisciani, 2009) or bound Jurassic-Cretaceous basins (e.g., Monte Bove area; Pierantoni et al., 2013). Other faults cut the contractional folds and were hence created after the Late Cenozoic contractional phase (e.g., the Mt. Vettore faults cutting through folds along the southern flank of Mt. Vettore itself). Also, it cannot be ruled out that some of the extensional faults showing postorogenic activity are reactivated (inherited) faults. While a full categorization of all faults of this region is beyond the scopes of this work, we simply subdivided them into *contractional* and *extensional*, explicitly omitting those structures whose kinematics were not indicated by the relevant investigators (Figure 10a).

Starting from this map, we constructed three geological sections: two perpendicular and one parallel to the strike of the activated faults (strike is taken from focal mechanisms; see Table 1). We used mesostructural data (e.g., the orientation of stratigraphic and structural surfaces) derived from Pierantoni et al. (2013) for the hanging wall area of the Sibillini Thrust, whereas for the footwall we used data from Centamore et al. (1992).

Section A (Figure 10b) crosses the northern part of the epicentral area close to the epicenter of the Norcia earthquake. From west to east, it shows an anticline-syncline pair dissected by high-angle extensional faults, several extensional faults that die out against the low-angle Sibillini thrust in the central part, and an anticline related to the development of an external thrust, that is, at the footwall of the Sibillini thrust.

Section B (Figure 10c) crosses the southern part of the epicentral area of the Norcia earthquake, and partially the northern part of the epicentral area of the Amatrice earthquake, running close to the lateral ramp of the Sibillini Thrust. It exhibits several high-angle extensional faults in the hanging wall of the Sibillini thrust, some of which are positively inherited from a preorogenic extensional phase, as testified by preserved horst and graben structures; others, such as the Mt. Vettore faults, cut contractional folds and hence are necessarily postorogenic. Two major folds lying in the footwall of the Sibillini thrust are likely connected with external compressional structures, such as the Acquasanta thrust.

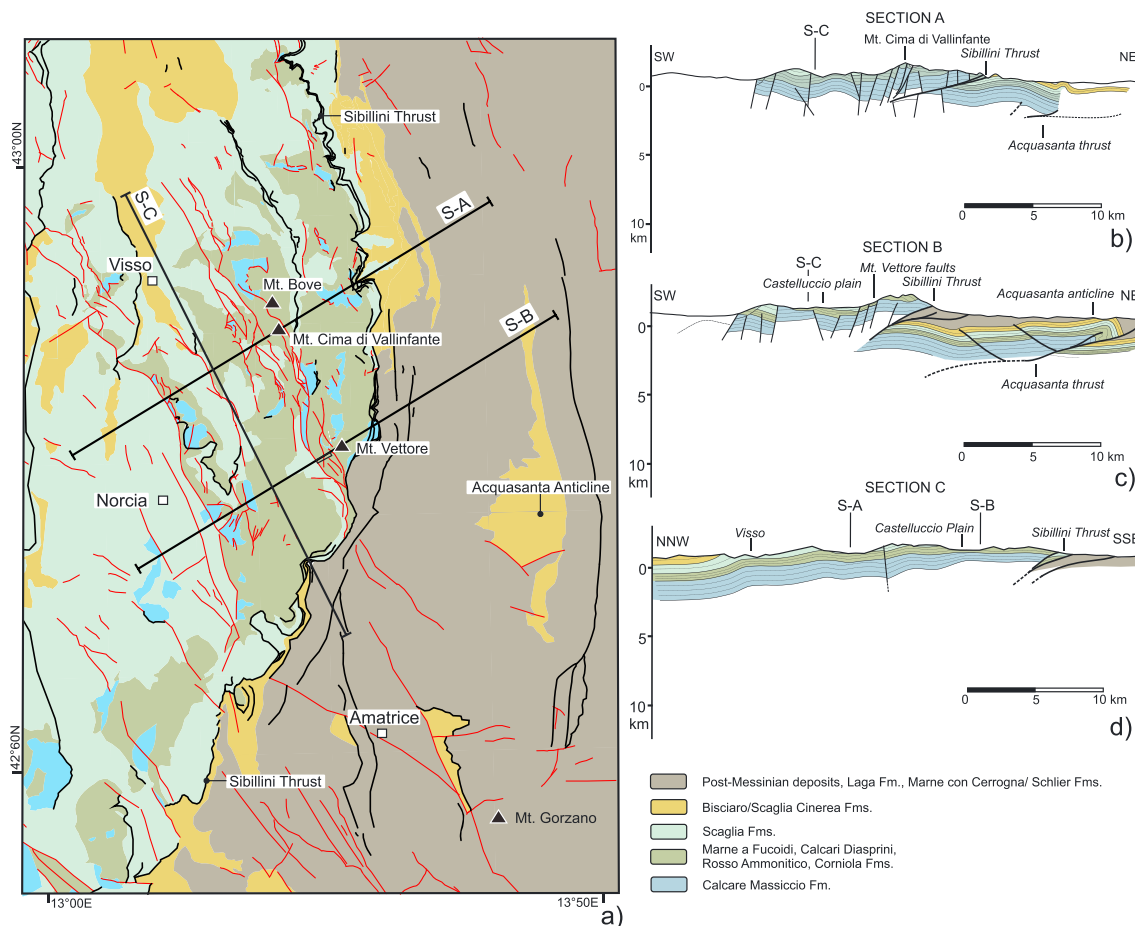


**Figure 10.** (a) Geology of the Amatrice-Norcia area showing the trace of the profiles used to construct the (b–d) shallow geological cross sections and to plot aftershock distributions (Figure 5). Faults shown on the map are only those for which literature sources indicated the presumed kinematics. The black and red lines represent reverse-thrust and normal faults, respectively. Sources: Servizio Geologico d'Italia (1941, 1952, 1955, 1958, 1963, 1965, 1966, 1967, 1968a, 1968ab, 1969, 1970), Bigi et al. (1992), Boncio et al. (2009), Centamore and Rossi (2009), Centamore et al. (1992), Cello et al. (1997), Giunta Regione Marche (2014), Mazzoli et al. (2005), Pierantoni et al. (2013), Pucci et al. (2017), Storti et al. (2017), Vezzani and Ghisetti (1998), and Vezzani et al. (2010).

Section C (Figure 10d) crosses the epicentral area of the Norcia earthquake from north to south. It shows a gentle deepening of the stratigraphic sequence from south to north. The *Calcare Massiccio* Fm. looks thinner in the southern zone because this area corresponds to a transitional zone between a paleo-structural high and a paleo-basin (Umbria-Marche Basin; see section 2), where this formation was partially removed by post-Jurassic submarine erosion. Few brittle structures are shown as most of them (especially major ones) strike roughly north-south, that is, parallel to the section. The lateral ramp of the Sibillini thrust is also well imaged.

### 5.3.2. 2-D Tectonic Models

We drew an interpretative tectonic model along each of the three profiles along which in the previous step we reconstructed the shallow geometries (Figure 10). The resulting three models encompass three options for the geometry of subsurface structures in the study region, based on the main geological uncertainties and interpretation rules discussed in section 5.2.

#### 5.3.2.1. Tectonic Model#1

In Tectonic Model#1 (Figure 11) the main décollement level is in the Triassic evaporites, and the tectonic slices are 3–5 km thick. The Hercynian basement lies at  $\approx 10$ -km depth and is not involved in the contraction (thin-skinned model). This model implies that the amount of orogenic shortening is large, that the flat portions of the thrust system are very long, and that the thrust ramps cut through the Jurassic-Cretaceous carbonates. In this model the Sibillini thrust is interpreted as a shallow structure with an out-of-sequence,

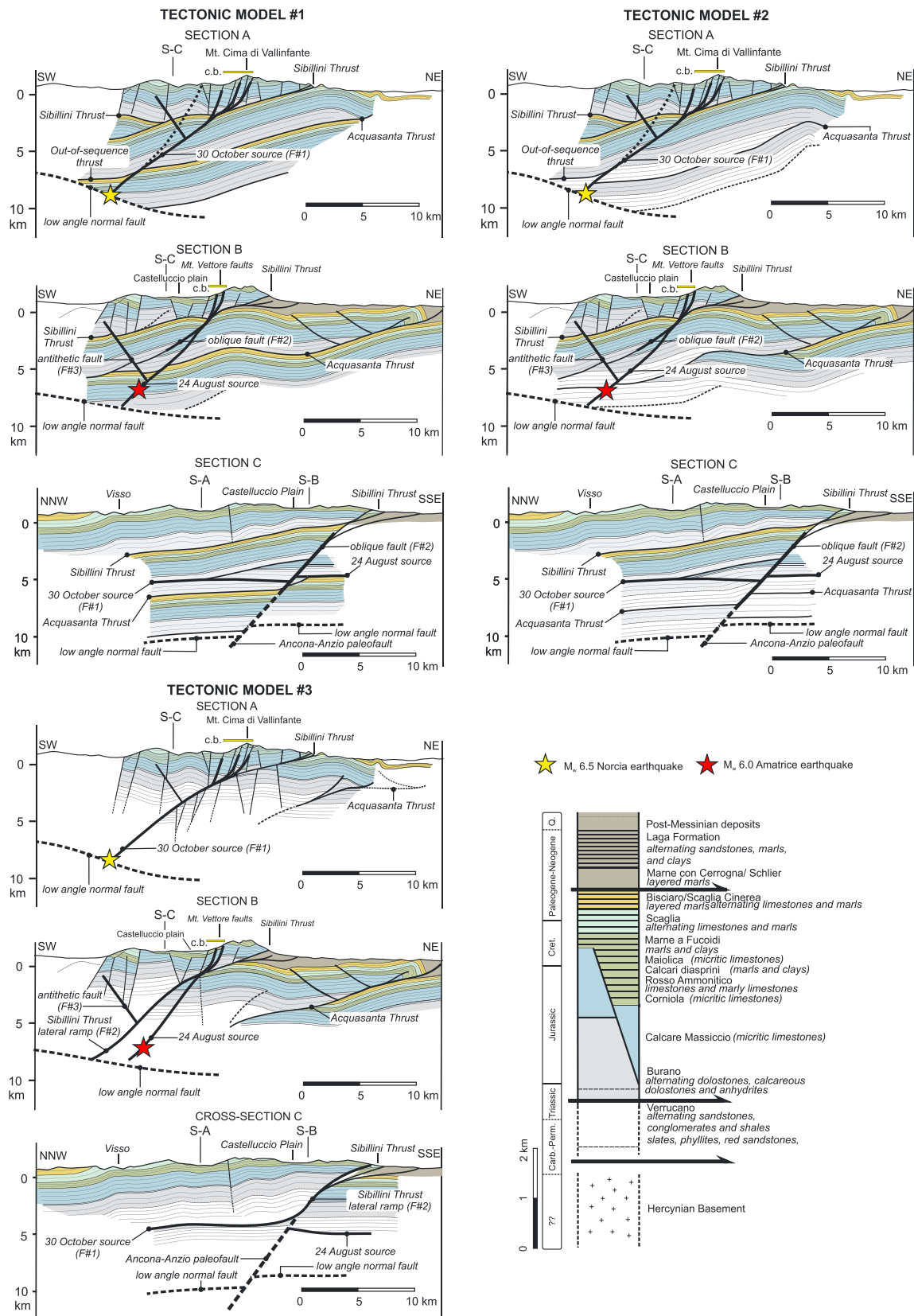


**Figure 11.** Tectonic models built starting from the three geological profiles shown in Figure 10. The thick black lines represent faults that participated in the earthquake sequence. The dotted black lines shown in all cross section A represent the trajectory of a postorogenic fault that does not use any inherited fault segment.

blind thrust ramp deflected toward the south to explain the existence of the two groups of contractional structures described in the area (see section 2.2). For delineating the contractional structures, we generally assumed a shear fault-bend fold model, except for the uppermost part of the Acquasanta Thrust, where we adopted a fault-propagation fold model.

In Tectonic Model#1 the hypothesized main seismogenic source crosses three complete stratigraphic successions, from the Triassic evaporites to Paleogene rocks. Section A (Figure 11) roughly runs across the location of the hypocenter of the Norcia earthquake. Even considering the inevitable uncertainties on the earthquake location, a relatively low-angle plane is necessary to connect the hypocenter to the roots of the high-angle surface faults that were reportedly activated following the 30 October shock (faults of the Cima di Vallinfante area in Figure 11). As a postorogenic extensional fault is expected to steepen when its plane crosses competent units, a postorogenic fault nucleating near the hypocenter and propagating upward (dotted black lines in Figure 11) should steepen when it crosses the competent rocks of the *Calcare Massiccio* Fm., lying at ~3- to 5-km depth). However, this occurrence would imply that an extensional fault intercepts the ground surface 2–3 km west of the reported coseismic surface breaks. To simultaneously intercept these breaks and the hypocenter, however, requires a rather low-angle structure (~40°), a common dip for reverse faults crossing competent rocks. Tectonic reconstructions based on thin-skinned models suggested the existence of a large-scale, out-of-sequence thrust located below the Sibillini Thrust (Barchi, 1991). Hence, we introduced this structure in our models so that part of its ramp can be reused to accommodate present-day extension while keeping a rather low-angle dip in the central zone of the Section A. Notice that the upper tip appears to have been deflected along the shallower Sibillini Thrust, as suggested by the criteria shown in section 5.2 (Figure 9).

The structural evolution of an extensional structure along the cross section can be summarized as follows:

1. A new extensional fault nucleated at 7- to 9-km depth.
2. During its upward propagation, this fault was deflected along an inherited reverse fault (thrust ramp), reusing its plane up to the intersection with the Sibillini Thrust.
3. New extensional fault splays nucleating in that focal point accommodated extension in the shallower part of the section, that is, above 2- to 3-km depth.

Section B (Figure 11) crosses the area where the seismogenic sources of the Norcia and Amatrice earthquakes are believed to overlap, as also suggested by the reported activation of surface faults (Monte Vettore faults) during both earthquakes. Based on this reconstruction the causative sources of the Amatrice and Norcia earthquakes share the same shallower structures. In the area of the Norcia earthquake, this tectonic model includes an oblique fault that partially reuses a lateral thrust ramp, the same thrust that was partially reused along Section A.

In both Sections A and B, the antithetic fault is interpreted as a new extensional fault that crosscuts inherited faults and accommodates hanging wall deformation in the Norcia and Amatrice areas.

Section C (Figure 11) shows clearly the oblique fault. To justify slip on a large extensional fault that is not properly oriented with respect to present-day extension, and that crosses incompetent rocks without showing an extensional fault-propagation fold mechanism, we resorted to inherited structures. The upper part of the oblique fault coincides with the expected location of the lateral ramp of both the Sibillini and the out-of-sequence thrusts. The dip of the latter ones is expected to be steeper than that of its frontal segment. Its deeper portion may coincide with a large inherited Mesozoic fault whose presence has been hypothesized in this area (Ancona-Anzio paleo-fault; see Di Domenica et al., 2014, and references therein).

Finally, between Sections A and B, the postorogenic extensional fault cannot reuse a large portion of the out-of-sequence thrust. This happens because a thin-skinned configuration implies that such thrust must gradually rotate strike-wise while approaching the lateral ramp.

#### **5.3.2.2. Tectonic Model #2**

In this model, the main décollement level is placed in the Permian rocks (Figure 11). Its general architecture does not differ much from that of Tectonic Model #1. However, there are at least two major differences: (a) the tectonic slices are thicker and (b) the deeper portion of the section (from 5- to 9-km depth) is composed by Permian-Triassic rocks. The adopted kinematic models are the same as those of the Tectonic Model#1, although the assumed orogenic shortening is lower. Also, the flat portion of the out-of-sequence thrust is

located at the base of Triassic evaporites because the limited displacement along the ramp makes a large thrust in incompetent rocks unlikely and would imply a large associated fold. The structures that we reconstructed in the shallower portion of the section did not suggest the existence of a contractional structure with large hanging wall uplift. Similar to Tectonic Model#1, in Section A (Figure 11) extensional reuse of an inherited segment is required to reduce the dip at intermediate depth. The roots of the new fault are now located in Permo-Triassic rocks. The architecture of Sections B and C (Figure 11) is very similar to that seen in Tectonic Model#1 except for their deeper portions, where faults cross Permian rocks, and for the tectonic significance of the oblique fault.

### 5.3.2.3. Tectonic Model #3

In this model (Figure 11) both the Hercynian basement and the overlying Permo-Triassic rocks are completely involved in the contraction (thick-skinned model). The structure is dominated by the Sibillini thrust, that in this model exhibits (a) a very low-angle, shallow ramp, and (b) a deeper and steeper ramp, coinciding with the main seismogenic source. In other words, this model assumes that the Norcia earthquake was caused by negative inversion of the steeper part of the Sibillini thrust. In this perspective, the exposed extensional faults would be synthetic, high-angle splays generated during the negative reactivation of the thrust ramp. The orogenic shortening is very small, and the two groups of contractional structures represent the complex expression of a single evolving stage, as suggested by Tavarnelli (1997). To reconstruct the main structure, we assumed a fault-bend fold model for the steeper ramp and a shear fault-bend fold model for the shallower ramp. In Section A (Figure 11), the small orogenic shortening allowed us to predict the location of the roots of the shortcut faults occurring in the hanging wall of the Sibillini Thrust. Sections B and C (Figure 11) show that the oblique fault coincides with the lateral ramp of this upper crustal thrust and that the antithetic fault is reminiscent of a back-thrust.

## 6. Discussion

Our approach to characterizing and discussing the source of the 30 October 2016,  $M_w$  6.5, Norcia earthquake combines the inversion of coseismic surface displacements retrieved from both DInSAR and GPS data with the modeling of the geological structure at seismogenic depth.

Tables 1 and 2 summarize the geometric and kinematic parameters published by numerous investigators, based on waveform inversion and the analysis of coseismic displacements, respectively. Seismological analyses from the literature return a fault dip fluctuating around  $40^\circ$ , an estimate also confirmed by analyses of the deformation field revealed by DInSAR data. A characteristic revealed by the DInSAR observations of the Norcia earthquake is the sizable positive LOS observed over a relatively large area around the city of Norcia (see orange areas in Figure 7), that is to say, in the hanging wall of the main southwest dipping earthquake causative fault. There are two fundamental ways to fit this characteristic pattern: (1) by using a rather low-angle dip for the main fault ( $\leq 40^\circ$ ), as initially suggested by Valensise et al. (2016) also based on a comparison with other normal faulting earthquakes that have occurred in the central Apennines over the past two decades, or (2) by increasing the number of independent faults.

On the one hand, multiple-fault models increase the degrees of freedom, inevitably resulting in a better fit to the data with respect to single-fault models; this condition, however, makes it more difficult to assess the relative merit of a simple versus more complex models. On the other hand, multiple-fault models inevitably imply that more than one fault ruptured during the mainshock or the early postseismic phase: this is a viable scenario, but also one that requires adequate seismological evidence for source complexity.

So far, numerous independent investigators have explored widely different fault models (Table 2). For instance, Cheloni et al. (2017), Scognamiglio et al. (2018), and Walters et al. (2018) explored several realizations of a multiple fault model by changing the geometry of the fault plane, and particularly its dip. Modeling the mainshock with a multifault model that includes the main southwest dipping fault (Fault#1 in our models) and an oblique fault (Fault#2 in our models) is relatively straightforward. Such an arrangement is simpler because the two synthetic planes are adjacent to one another, allowing the mainshock rupture to propagate from the hypocenter to the oblique fault easily (see rupture model imaged by inverting ground velocity time histories in Scognamiglio et al., 2018). Envisioning the simultaneous activation of an additional antithetic fault (e.g., Fault#3 in our models) during the mainshock is more problematic. There exist various examples of normal faulting earthquake sequences involving slip on antithetic faults (e.g., the 1980, Irpinia,

Southern Italy,  $M_w$  6.8, and the 1984 Devils Canyon, Idaho,  $M_w$  5.8 earthquake sequences), but the nucleation of seismic ruptures along such faults is commonly observed well after the main rupture (e.g., Bruhn & Schults, 1996). So far, none of the seismological analyses highlighted a delayed rupture along an antithetic fault in the Norcia 2016 sequence. As we mentioned earlier, the time distribution of aftershocks suggests that the antithetic fault imaged by the aftershock pattern (Fault#3 in our models) was the locus of background seismicity soon after the 24 August Amatrice earthquake, that is, 2 months before the 30 October shock. Besides, as shown by our results as well as by other published models (e.g., Walters et al., 2018), the amount of slip occurring on the antithetic fault is not crucial for fitting the surface displacements.

Another open question is the dip of the oblique fault (Fault#2 in our models). Cheloni et al. (2017) assumed a  $30^\circ$  dip (Table 2) in order to fit the deformations observed in the Norcia area. They justified this choice by assuming that this low-angle fault is an ancillary structure, and specifically that it corresponds with the lateral ramp of the Sibillini thrust in a thin-skinned configuration. The same investigators, however, acknowledged that their proposed oblique fault does not show any aftershocks associated with it and suggested that it slipped aseismically generating the equivalent of an  $M_w \sim 6.1\text{--}6.2$  earthquake. In our model, in agreement with other investigators (e.g., Scognamiglio et al., 2018; Walters et al., 2018), the dip of oblique fault was set at  $40\text{--}50^\circ$  (see Tables 2 and 3), which allows for a good fit of the aftershock distribution.

A further open question concerning the multiple-fault model is the southeastward extension of the main fault: does it extend beyond the intersection with the oblique fault, which would then fall in its hanging wall, or does it stop against it? Our geodetic modeling has shown that in the first case coseismic slip increases along the oblique fault and decreases along the main fault (Figure 6). All other studies modeled only scenarios where the main fault extends beyond the junction with the oblique fault (e.g., Scognamiglio et al., 2018; Walters et al., 2018), similar to our first three geodetic models. In the second case, that is, with the main fault confined by the oblique fault, our modeled slip decreased along the oblique fault and is more coherent with the rake calculated using other techniques (e.g., focal mechanisms; Table 1).

Let us now elucidate the question of fault dip from a strictly geological point of view. In all our tectonic models we proposed different solutions constraining fault dip at a rather low angle; to stress this even further, in the first two models we proposed the reuse of portions of inherited contractional structures, which are inherently low angle. We justified this choice with the need to connect the hypocenter to the coseismic surface break while fitting the aftershock distribution. This circumstance arises because thin-skinned models predict the existence of two or three levels of competent rocks that would imply a steepening of the main fault plane. Are there other mechanisms that may explain the existence of new faults forming at low-angle? Are these mechanisms coherent with the tectonic setting of this area? A rather shallow dip for the main seismogenic plane may seem anomalous in view of Anderson's faulting theory that predicts a much steeper dip for a new extensional fault ( $\approx 60^\circ$ ; Anderson, 1951). However, there exist at least two additional reasons why a normal fault could be generated at low-angle, aside from the mechanical characteristics of the host rocks: (a) a rotation to a lower dip in a domino model, as seen in the Basin-and-Range province of the Western United States (e.g., Kusznir & Ziegler, 1992), or (b) a departure from vertical of the maximum stress axis, that forms an angle with the Earth surface (e.g., Westaway, 1999). Solution a; domino rotation) must be discarded, as it implies very long fault activity under the same stress regime, a condition that hardly applies to the central Apennines, where extension reached the area under study in relatively recent times. Solution (b) (non-Andersonian mechanism due to  $\sigma_1$  not perpendicular to the Earth surface) would require the regional  $\sigma_1$  to rotate westward by about  $20^\circ$ . In its turn, this would require a geodynamic mechanism producing west directed traction at the base of the lithosphere. Geodynamic models of the Apennines, however, do suggest the existence of lithospheric basal tractions imposed by the mantle flow, but in the opposite direction, that is, eastward (e.g., Barba et al., 2008; Doglioni et al., 1999; Finocchio et al., 2016). Hence, also the rotation of the  $\sigma_1$  can hardly be invoked to justify the low-angle dip of the main extensional fault.

In summary, it is hard to find a simple mechanical solution that justifies the shallow dip of the main fault without invoking a re-utilization of inherited fault segments. In our Model#3 (Figure 11), obtaining a shallow-dipping master fault was simple because the seismogenic fault is assumed to coincide with a former thrust ramp, and a dip of  $37\text{--}40^\circ$  is close enough to Anderson's prediction for a reverse fault in an undisturbed material ( $\approx 30^\circ$ ). Simple mechanisms can be invoked to increase an Andersonian dip during

contraction; for instance, the interference of the ramp with external thrusts (e.g., the Acquasanta Thrust). Other Apennines thrust ramps that developed in a similar stratigraphic sequence do exhibit a dip of 30–50°; for instance, in the recent May 2012, Emilia reverse faulting earthquake sequence, the two  $M_w$  6.1–5.9 mainshocks were generated by thrust ramps respectively dipping 40 and 45° (e.g., Bonini, Toscani, & Seno, 2014; Maesano et al., 2015; Vannoli et al., 2015).

A major issue for Model#3 is the mechanical feasibility of the negative inversion of a thrust ramp. Global compilations of the dip of large active faults (e.g., Collettini & Sibson, 2001), on the one hand, and rock mechanics considerations, on the other hand, suggest that the extensional activation of a fault is feasible down to a dip of 30° (e.g., Collettini & Sibson, 2001). Hence, a (partial?) negative reactivation of inherited thrust ramps in the extensional portions of the Apennines is indeed a viable scenario that deserves full consideration.

A final remark concerns the nature of the oblique fault. All our tectonic models require the reuse of inherited faults, a circumstance that would justify the reactivation of a large extensional fault that is rather misoriented with respect to the present-day extension. Other investigators have already suggested that this structure is an inherited fault reactivated as a transtensional fault (e.g., Bonini, Basili, et al., 2016; Falcucci et al., 2018; Scognamiglio et al., 2018).

## 7. Conclusions

The occurrence of the 30 October 2016,  $M_w$  6.5, Norcia earthquake, the largest shock of the 2016–2017 central Italy sequence, spurred many important investigations, yet it left some fundamental question unanswered: what is the nature of the earthquake causative fault? Is it (a) a relatively youthful fault, cutting through the highly complex fabric of this portion of the Apennines fold-and-thrust belt; (b) a fault obtained by negative inversion of the Sibillini thrust, one of the largest contractional structures of peninsular Italy; or (c) does it represent some combination of these two end members? In this work, we addressed this outstanding question, and we did not find convincing evidence that the causative fault of the Norcia earthquake entirely developed during postorogenic extension. Aside from the dominant tectonic scheme that one may decide to adopt in this region (e.g., thin- vs. thick-skinned; see section 6), a partial or total reuse of inherited structures is mandatory to fit all data satisfactorily, and especially to satisfy the rather low-angle dip that we obtained from our geodetic models (~37°) and previously published estimates (40°; Table 1). In this framework, the spectacular surface breaks caused by the Norcia earthquake would be the result of the activation of steeper shallow faults overlying a master fault.

We maintain that a multiple-fault model composed by a main fault parallel to the prevalent strike inferred from focal mechanism solutions, confined to the southeast by an oblique fault, is the most convincing solution for matching all the available evidence, for instance, the obliquity of the rake and the dip of the main fault (Table 1 and section 5).

Our findings may have crucial implications for the seismogenic potential of other tectonically similar settings that are encountered to the east-northeast of the main Apennines backbone, *en route* between the Maiella massif, in the Abruzzi Apennines, to the south, and the Marche and Romagna Apennines, to the north. In these external areas, the tectonic extension is substantially younger than in the inner portions of the chain, and it is hence more prone to be overlooked or drastically underestimated. We also stress the need to cope with the complexity of active tectonic processes in peninsular Italy by always resorting to a harmonized blend of instrumental, seismotectonic, and geological observations.

## References

- Albertz, M., & Sanz, P. F. (2012). Critical state finite element models of contractional fault-related folding: Part 2. Mechanical analysis. *Tectonophysics*, 576–577, 150–170. <https://doi.org/10.1016/j.tecto.2012.06.016>
- Alvarez, W., Coccozza, T., & Wezel, F.-C. (1974). Fragmentation of the Alpine belt my microplate dispersal. *Nature*, 248(5446), 309–314. <https://doi.org/10.1038/248309a0>
- Anderson, E. M. (1951). *The dynamics of faulting and dyke formation with application to Britain* (2nd ed., p. 206). Edinburgh: Oliverand Boyd.
- Anelli, L., Gorza, M., Pieri, M., & Riva, M. (1994). Subsurface well data in the Northern Apennines (Italy). *Memorie della Societa Geologica Italiana*, 48, 461–471.
- Bagnoli, G., Gianelli, G., Puxeddu, M., Rau, A., Squarci, P., & Tongiorgi, M. (1979). A tentative stratigraphic reconstruction of the Tuscan Paleozoic basement. *Memorie della Societa Geologica Italiana*, 20, 99–116.

### Acknowledgments

This work was supported by INGV R.U. 0865.050, P.I. U. Fracassi, of Project MIUR-FISR 2016 “Centro di studio e monitoraggio dei rischi naturali dell’Italia centrale,” and by “Finanziamenti di Ateneo per Progetti Scientifici” -FRA 2015, P.I. L. Bonini. Petroleum Expert Ltd is acknowledged for making available the Move software to the the University of Trieste. We thank Christian Bignami and Cristiano Tolomei for distributing online the deformation fields obtained through their DInSAR data processing. The Editor John Geissman, an anonymous Associated Editor, reviewer Ken McCaffrey, and two anonymous reviewers are gratefully acknowledged for their reviews and the constructive criticism that improved the quality of this paper. No new data were used in this manuscript.



- Bally, A., Burbi, L., Cooper, G., & Ghelardoni, R. (1986). Balanced sections and seismic reflection profiles across the Central Apennines. *Atti 73° Congr. Soc. Geol. Ital., "Geologia dell'Italia centrale"*. *Memorie della Società Geologica Italiana*, 35, 257–310.
- Barba, S., Carafa, M. M. C., & Boschi, E. (2008). Experimental evidence for mantle drag in the Mediterranean. *Geophysical Research Letters*, 35, L06302. <https://doi.org/10.1029/2008GL033281>
- Barchi, M. (1991). Integration of a seismic profile and surface geology in a cross section through the Umbria-Marche Apennines. *Bollettino della Società Geologica Italiana*, 110(3–4), 469–479.
- Barchi, M., De Feyter, A., Magnani, M. B., Minelli, G., & Piali, G. (1998). The structural style of the Umbria-Marche fold and thrust belt. *Memorie della Società Geologica Italiana*, 52(527), 38.
- Basili, R., & Barba, S. (2007). Analysis of seismological and geological observations for moderate-size earthquakes: The Colfiorito Fault System (Central Apennines, Italy). *Geophysical Journal International*, 141(1), 241–252. <https://doi.org/10.1046/j.1365-246X.2000.00080.x>
- Bernoulli, D., & Jenkyns, H. C. (1974). Alpine, Mediterranean, and central Atlantic Mesozoic facies in relation to the early evolution of the Tethys. In R. H. Dott Jr. & R. H. Shaver (Eds.), *Modern and Ancient Geosynclinal Sedimentation Special Publication* (Vol. 19, pp. 129–160). Society of Economic Paleontologists and Mineralogists.
- Bigi, G., Cosentino, D., Parotto, M., Sartori, R., Scandone, P. (1992). Structural model of Italy. Scala 1:500,000. C.N.R., Progetto Finalizzato Geodinamica, Sottoprogetto: Modello strutturale tridimensionale. Quaderni Ric. Scient., 114, 3.
- Bignami, C. (2017). Ground deformation maps of the Visso and Norcia 2016 earthquakes captured from Sentinel-1 SAR [Data set]. <https://doi.org/10.5281/zenodo.545818>
- Billi, A., Tiberti, M. M., Cavinato, G. P., Cosentino, D., Di Luzio, E., Keller, J. V. A., et al. (2006). First results from the CROP-11 deep seismic profile, central Apennines, Italy: Evidence of mid-crustal folding. *Journal of the Geological Society*, 163(4), 583–586. <https://doi.org/10.1144/0016-764920-002>
- Boccaletti, M., Coli, M., Decandia, F. A., Giannini, E., & Lazzarotto, A. (1981). Evoluzione dell'Appennino Settentrionale secondo un nuovo modello strutturale. *Memorie della Società Geologica Italiana*, 21, 359–373.
- Bonanno, E. (2018). Fault-propagation fold kinematics in mechanically anisotropic rocks: controlling factors. Università di Pavia. Ph.D. Thesis.
- Bonanno, E., Bonini, L., Basili, R., Toscani, G., & Seno, S. (2017). How do horizontal, frictional discontinuities affect reverse fault-propagation folding? *Journal of Structural Geology*, 102, 147–167. <https://doi.org/10.1016/j.jsg.2017.08.001>
- Bonarelli, G. (1899). Escursioni della Società Geologica Italiana nei dintorni di Ascoli Piceno. *Bollettino della Società Geologica Italiana*, 18(1), 58–67.
- Boncio, P., Tinari, D. P., Lavecchia, G., Misini, F., & Milana, G. (2009). The instrumental seismicity of the Abruzzo Region in Central Italy (1981–2003): Seismotectonic implications. *Italian Journal of Geosciences*, 128(2), 367–380. <https://doi.org/10.3301/IJG.2009.128.2.367>
- Bonini, L., Basili, R., Toscani, G., Burrato, P., Seno, S., & Valensise, G. (2015). The role of pre-existing discontinuities in the development of extensional faults: An analog modeling perspective. *Journal of Structural Geology*, 74, 145–158. <https://doi.org/10.1016/j.jsg.2015.03.004>
- Bonini, L., Basili, R., Toscani, G., Burrato, P., Seno, S., & Valensise, G. (2016). The effects of pre-existing discontinuities on the surface expression of normal faults: Insights from wet clay analog modeling. *Tectonophysics*, 684, 157–175. <https://doi.org/10.1016/j.tecto.2015.12.015>
- Bonini, L., Di Bucci, D., Toscani, G., Seno, S., & Valensise, G. (2014). On the complexity of surface ruptures during normal faulting earthquakes: Excerpts from the 6 April 2009 L'Aquila (central Italy) earthquake (Mw 6.3). *Solid Earth*, 5(1), 389–408. <https://doi.org/10.5194/se-5-389-2014>
- Bonini, L., Maesano, F. E., Basili, R., Burrato, P., Carafa, M. M. C., Fracassi, U., et al. (2016). Imaging the tectonic framework of the 24 August 2016, Amatrice (central Italy) earthquake sequence: New roles for old players? *Annals of Geophysics*, 59(5). <https://doi.org/10.4401/ag-7229>
- Bonini, L., Toscani, G., & Seno, S. (2014). Three-dimensional segmentation and different rupture behaviour during the 2012 Emilia seismic sequence (northern Italy). *Tectonophysics*, 630, 33–42. <https://doi.org/10.1016/j.tecto.2014.05.006>
- Brandes, C., & Tanner, D. C. (2014). Fault-related folding: A review of kinematic models and their application. *Earth-Science Review*, 138, 352–370. <https://doi.org/10.1016/j.earscirev.2014.06.008>
- Bruhn, R. L., & Schults, R. A. (1996). Geometry and slip distribution in normal fault systems: Implications for mechanics and fault-related hazards. *Journal of Geophysical Research*, 101(B2), 3401–3412. <https://doi.org/10.1029/95JB03253>
- Calamita, F., & Deiana, G. (1988). The arcuate shape of the Umbria-Marche-Sabina Apennines (Central Italy). *Tectonophysics*, 146(1–4), 139–147. [https://doi.org/10.1016/0040-1951\(88\)90087-X](https://doi.org/10.1016/0040-1951(88)90087-X)
- Calamita, F., Pace, P., & Satolli, S. (2012). Coexistence of fault-propagation and fault-bend folding in curve-shaped foreland fold-and-thrust belts: Examples from the Northern Apennines (Italy). *Terra Nova*, 24(5), 396–406. <https://doi.org/10.1111/j.1365-3121.2012.01079.x>
- Calamita, F., Satolli, S., Scisciani, V., Esestime, P., & Pace, B. (2011). Contrasting styles of fault reactivation in curved orogenic belts: Examples from the Central Apennines (Italy). *Geological Society of America Bulletin*, 123(5–6), 1097–1111. <https://doi.org/10.1130/B30276.1>
- Castellarin, A., Colacicchi, M., Praturlon, A., & Cantelli, C. (1982). The Jurassic-Lower Pliocene history of the Ancona-Anzio line (Central Italy). *Memorie della Società Geologica Italiana*, 24, 325–336.
- Castellarin, A., Colacicchi, R., & Praturlon, A. (1978). Fasi distensive, trascorrenze e sovrascorrimenti lungo la "linea Ancona-Anzio" dal Lias medio al Pliocene. *Geologica Romana*, 27, 161–189.
- Cavinato, G. P., Salvini, F., & Tozzi, M. (1986). Evoluzione strutturale del settore centrale della Linea Olevano-Antrdoco. *Memorie della Società Geologica Italiana*, 35, 591–601
- Cello, G., Mazzoli, S., Tondi, E., & Turco, E. (1997). Active tectonics in the central Apennines and possible implications for seismic hazard analysis in peninsular Italy. *Tectonophysics*, 272(1), 43–68. [https://doi.org/10.1016/S0040-1951\(96\)00275-2](https://doi.org/10.1016/S0040-1951(96)00275-2)
- Centamore, E., Adamoli, L., Berti, D., Bigi, G., Bigi, S., Casnedi, R., et al. (1992). *Carta geologica dei bacini della Laga e del Cellino e dei rilievi carbonatici circostanti*. Firenze: S.El.Ca.
- Centamore, E., & Rossi, D. (2009). Neogene-Quaternary tectonics and sedimentation in the Central Apennines. *Italian Journal of Geosciences*, 128(1), 73–88.
- Chamberlin, T. C. (1965). The method of multiple working hypotheses. *Science*, 148(3671), 754–759. <https://doi.org/10.1126/science.148.3671.754>
- Cheloni, D., De Novellis, V., Albano, M., Antonioli, A., Anzidei, M., Atzori, S., et al. (2017). Geodetic model of the 2016 Central Italy earthquake sequence inferred from InSAR and GPS data. *Geophysical Research Letters*, 44, 6778–6787. <https://doi.org/10.1002/2017GL073580>

- Chiarabba, C., De Gori, P., Cattaneo, M., Spallarossa, D., & Segou, M. (2018). Faults geometry and the role of fluids in the 2016-2017 Central Italy seismic sequence. *Geophysical Research Letters*, *45*, 6963–6971. <https://doi.org/10.1029/2018GL077485>
- Chiaraluca, L., Di Stefano, R., Tinti, E., Scognamiglio, L., Michele, M., Casarotti, E., et al. (2017). The 2016 Central Italy seismic sequence: A first look at the mainshocks, aftershocks, and source models. *Seismological Research Letters*, *88*(3), 757–771. <https://doi.org/10.1785/0220160221>
- Civico, R., Pucci, S., Villani, F., Pizzimenti, L., De Martini, P. M., Nappi, R., & the Open EMERGEO Working Group (2018). Surface ruptures following the 30 October 2016 Mw 6.5 Norcia earthquake, central Italy. *Journal of Maps*, *14*(2), 151–160. <https://doi.org/10.1080/17445647.2018.1441756>
- Colletini, C., & Sibson, R. H. (2001). Normal fault, normal friction? *Geology*, *29*(10), 927–930. [https://doi.org/10.1130/0091-7613\(2001\)029<0927:NFNF>2.0.CO;2](https://doi.org/10.1130/0091-7613(2001)029<0927:NFNF>2.0.CO;2)
- Dahlstrom, C. D. A. (1969). Balanced cross sections. *Canadian Journal of Earth Sciences*, *6*(4), 743–757. <https://doi.org/10.1139/e69-069>
- Dewey, J. F., Helman, M. L., Turco, E., Hutton, D. H. W., & Knott S. D. (1989). “Kinematics of the western Mediterranean.” In M. P. Coward, D. Dietrich, R. G. Park (Eds.), *Alpine tectonics, Geological Society Special Publication* (Vol. 45, pp. 265–283). <https://doi.org/10.1144/GSL.SP.1989.045.01.15>
- Di Domenico, A., Bonini, L., Calamita, F., Toscani, G., Galuppo, C., & Seno, S. (2014). Analogue modeling of positive inversion tectonics along differently oriented pre-thrusting normal faults: An application to the Central-Northern Apennines of Italy. *Geological Society of America Bulletin*, *126*(7–8), 943–955. <https://doi.org/10.1130/B31001.1>
- Di Luzio, E., Mele, G., Tiberti, M. M., Cavinato, G. P., & Parotto, M. (2009). Moho deepening and shallow upper crustal delamination beneath the central Apennines. *Earth and Planetary Science Letters*, *280*(1–4), 1–12. <https://doi.org/10.1016/j.epsl.2008.09.018>
- Dogliani, C., Anzidei, M., Pondrelli, S., & Florindo, F. (2016). The Amatrice seismic sequence: preliminary data and results. Preface. *Annals of Geophysics*, *59*(5).
- Dogliani, C., Harabaglia, P., Merlini, S., Mongelli, F., Peccerillo, A., & Piromallo, C. (1999). Orogens and slabs vs their direction of subduction. *Earth Science Reviews*, *45*(3–4), 167–208. [https://doi.org/10.1016/S0012-8252\(98\)00045-2](https://doi.org/10.1016/S0012-8252(98)00045-2)
- EMERGEO Working Group (2016). Coseismic effects of the 2016 Amatrice seismic sequence: First geological results. *Annals of Geophysics*, *59*(5). <https://doi.org/10.4401/ag-7195>
- Falucci, E., Gori, S., Bignami, C., Pierantonio, G., Melini, D., Moro, M., et al. (2018). The Campotosto seismic gap in between the 2009 and 2016-2017 seismic sequence of central Italy and the role of inherited lithospheric faults in regional seismotectonic settings. *Tectonics*, *37*, 2425–2445. <https://doi.org/10.1029/2017TC004844>
- Ferril, D. A., Morris, A. P., McGinnins, R. N., Smart, K. J., Wigginton, S. S., & Hill, N. J. (2017). Mechanical stratigraphy and normal faulting. *Journal of Structural Geology*, *94*, 275–302. <https://doi.org/10.1016/j.jsg.2016.11.010>
- Finocchio, D., Barba, S., & Basili, R. (2016). Slip rate depth distribution for active faults in Central Italy using numerical models. *Tectonophysics*, *687*, 232–244. <https://doi.org/10.1016/j.tecto.2016.07.031>
- Fletcher, R. C., & Pollard, D. D. (1999). Can we understand structural and tectonic processes and their products without appeal to a complete mechanics? *Journal of Structural Geology*, *21*(8–9), 1071–1088. [https://doi.org/10.1016/S0191-8141\(99\)00056-5](https://doi.org/10.1016/S0191-8141(99)00056-5)
- Ghisetti, F., & Vezzani, L. (1997). Interfering paths of deformation and development of arcs in the fold-and-thrust belt of the central Apennines (Italy). *Tectonics*, *16*(3), 523–536. <https://doi.org/10.1029/97TC00117>
- Giunta Regione Marche (2014). Carta delle litologie Scala 1:100.000 – Regione Marche, Servizio Infrastrutture, Trasporti e Energia, P.F. Urbanistica, Paesaggio e Informazioni Territoriali.
- Groshong, R. H. Jr., Bond, C., Gibbs, A., Ratliff, R., & Wiltshcko, D. V. (2012). Preface: Structural balancing at the start of the 21st century: 100 years since Chamberlin. *Journal of Structural Geology*, *41*, 1–5. <https://doi.org/10.1016/j.jsg.2012.03.010>
- Hughes, A. N., & Shaw, J. H. (2014). Fault displacement distance relationships as indicators of contraction fault-related folding style. *AAPG Bulletin*, *98*(2), 227–251. <https://doi.org/10.1306/05311312006>
- Hughes, A. N., & Shaw, J. H. (2015). Insights into the mechanics of fault-propagation folding styles. *Geological Society of America Bulletin*, *127*(11–12), 1752–1765. <https://doi.org/10.1130/B31215.1>
- INGV Geodesy Working Group (2016). Preliminary co-seismic displacements for the October 26 (Mw 5.9) and October 30 (Mw 6.5) central Italy earthquakes from the analysis of GPS stations. <https://doi.org/10.5281/zenodo.167959>
- Koopman, A. (1983). Detachment tectonics in the Central Apennines. *Geologica Ultraiectina*, *30*, 1–55.
- Kusznir, N. J., & Ziegler, P. A. (1992). The mechanics of continental extension and sedimentary basin formation: A simple-shear/pure-shear flexural cantilever model. *Tectonophysics*, *215*(1–2), 117–131. [https://doi.org/10.1016/0040-1951\(92\)90077-J](https://doi.org/10.1016/0040-1951(92)90077-J)
- Lavecchia, G. (1985). Il sovrascorrimento dei Monti Sibillini: analisi cinematica e strutturale. *Bollettino della Società Geologica Italiana*, *104*(1), 161–194.
- Lavecchia, G., Minelli, G., & Pialli, G. (1983). Strutture plicative minori dell'Appennino Umbro-Marchigiano. *Bollettino della Società Geologica Italiana*, *102*, 95–112.
- Lawson, C. L., & Hanson, R. J. (1974). *Solving least squares problems, Series in Automatic Computation* (p. 340). Englewood Cliffs, NJ: Prentice-Hall.
- Liu, C., Zhengm, Y., Xie, Z., & Xiong, X. (2017). Ruptures features of the  $M_w$  6.2 Norcia earthquake and its possible relationship with strong seismic hazards. *Geophysical Research Letters*, *44*, 1320–1328. <https://doi.org/10.1002/2016GL071958>
- Locardi, E. (1988). The origin of the Apenninic Arcs. In: Wezel, F.C. (Ed.), The Origin and Evolution of Arcs. *Tectonophysics*, *146*(1–4), 105–123. [https://doi.org/10.1016/0040-1951\(88\)90085-6](https://doi.org/10.1016/0040-1951(88)90085-6)
- Maesano, F. E., D'Ambrogio, C., Burrato, P., & Toscani, G. (2015). Slip-rates of blind thrusts in slow deforming areas: Examples from the Po Plain (Italy). *Tectonophysics*, *643*, 8–25. <https://doi.org/10.1016/j.tecto.2014.12.007>
- Malinverno, A., & Ryan, W. B. F. (1986). Extension of the Tyrrhenian Sea and shortening in the Apennines as result of a migration driven by sinking lithosphere. *Tectonics*, *5*(2), 227–245. <https://doi.org/10.1029/TC0051002p00227>
- Martinis, B., & Pieri, M. (1964). Alcune notizie sulla formazione evaporitica del Triassico Superiore nell'Italia centrale e meridionale. *Memorie della Società Geologica Italiana*, *4*(1), 649–678.
- Martino, S., Bozzano, F., Caporossi, P., D'angiò, D., Della Seta, M., Esposito, C., et al. (2017). Ground effects triggered by the 24th August 2016, Mw 6.0 Amatrice (Italy) earthquake: Surveys and inventorying to update the CEDIT catalogue. *Geografia Fisica e Dinamica Quaternaria*, *40*(1), 77–95. <https://doi.org/10.4461/GFDQ.2017.40.7>
- Mazzoli, S., Deiana, G., Galdenzi, S., & Cello, G. (2002). Miocene fault controlled sedimentation and thrust propagation in the previously faulted external zones of the Umbria–Marche Apennines, Italy. In G. Bertotti, K. Schulmann, & S. A. P. L. Cloetingh (Eds.), *Continental Collision and the tectono-sedimentary evolution of forelandsEurop. Geosc. Un. Stephan Mueller Spec. Publ. Ser.* (Vol. 1, pp. 195–209). <https://doi.org/10.5194/smsps-1-195-2002>

- Mazzoli, S., Pierantoni, P., Borraccini, F., Paltrinieri, W., & Deiana, G. (2005). Geometry, segmentation pattern and displacement variations along a major Apennine thrust zone, central Italy. *Journal of Structural Geology*, 27(11), 1940–1953. <https://doi.org/10.1016/j.jsg.2005.06.002>
- Mirabella, F., Barchi, M. R., Lupatelli, A., Stucchi, E., & Ciaccio, M. G. (2008). Insights on the seismogenic layer thickness from the upper crust structure of the Umbria-Marche Apennines (central Italy). *Tectonics*, 27, TC1010. <https://doi.org/10.1029/2007TC002134>
- Mirabella, F., Brozzetti, F., Lupatelli, A., & Barchi, M. R. (2011). Tectonic evolution of a low-angle extensional fault system from restored cross-sections in the Northern Apennines (Italy). *Tectonics*, 30, TC6002. <https://doi.org/10.1029/2011TC002890>
- Okada, Y. (1992). Internal deformation due to shear and tensile faults in a half space. *Bulletin of the Seismological Society of America*, 82, 1018–1040.
- Papadopoulos, G. A., Ganas, A., Agalos, A., Papageorgiou, A., Triantafyllou, I., Kontoes, C., et al. (2017). Earthquake Triggering Inferred from Rupture Histories, DInSAR Ground Deformation and Stress-Transfer Modelling: The Case of Central Italy During August 2016–January 2017. *Pure and Applied Geophysics*, 174, 3689–3711. <https://doi.org/10.1007/s00024-017-1609-8>
- Parotto, M., & Pratlurion, A. (1975). Geological summary of the Central Apennines. In L. Ogniben, M. Parotto, & A. Pratlurion (Eds.), *Structural model of Italy. Quaderni della Ricerca Scientifica* (Vol. 90, pp. 257–311). Rome: Consiglio Nazionale delle Ricerche.
- Patacca, E., & Scandone, P. (1989). Post Tortonian mountain building in the Apennines. The role of the passive sinking of a relict lithospheric slab. In A. Boriani (Ed.), *The lithosphere in Italy: Advances in Earth science research*. Ital. Nat. Comm. Int. Lith. Progr., Mid-term Conf. *Atti Conv. Lincei* (Vol. 80, pp. 157–176).
- Patacca, E., Scandone, P., Di Luzio, E., Cavinato, G. P., & Parotto, M. (2008). Structural architecture of the central Apennines: Interpretation of the CROP 11 seismic profile from the Adriatic coast to the orographic divide. *Tectonics*, 27, TC3006. <https://doi.org/10.1029/2005TC001917>
- Pavlidis, S., Chatzipetros, A., & Papanthasiou, G. (2017). Ground deformation and fault modeling of the 2016 sequence (24 Aug.–30 Oct.) in central Apennines (Central Italy). *Bulletin of the Geological Society of Greece*, 51,
- Pierantoni, P., Deiana, G., & Galdenzi, S. (2013). Stratigraphic and structural features of the Sibillini Mountains (Umbria-Marche Apennines, Italy). *Italian Journal of Geosciences*, 132(3), 497–520. <https://doi.org/10.3301/IJG.2013.08>
- Pizzi, A., Di Domenica, A., Gallovic, F., Luzi, L., & Puglia, R. (2017). Fault segmentation as constraint to the occurrence of the main shocks of the 2016 Central Italy seismic sequence. *Tectonics*, 36, 2370–2387. <https://doi.org/10.1002/2017TC004652>
- Porreca, M., Minelli, G., Ercoli, M., Brobia, A., Mancinelli, P., Cruciani, F., Giorgetti, C., et al. (2018). Seismic reflection profiles and sub-surface geology of the area interested by 2016–2017 earthquake sequence (Central Italy). *Tectonics*, 37, 1116–1137. <https://doi.org/10.1002/2017TC004915>
- Pucci, S., De Martini, P. M., Civico, R., Villani, F., Nappi, R., Ricci, T., et al. (2017). Coseismic ruptures of the 24 August 2016, Mw 6.0 Amatrice earthquake (central Italy). *Geophysical Research Letters*, 44, 2138–2147. <https://doi.org/10.1002/2016GL071859>
- Ricci Lucchi, F. (1986). The Oligocene to recent foreland basin of the Northern Apennines. In P. A. Allen, & P. Homewood (Eds.), *Foreland basins Intern. Ass. Sedim. Spec. Publ.* (Vol. 8, pp. 105–139).
- Roering, J. J., Cooke, M. L., & Pollard, D. D. (1997). Why blind thrust faults do not propagate to the Earth's surface: Numerical modeling of coseismic deformation associated with thrust-related anticlines. *Journal of Geophysical Research*, 102(B6), 11,901–11,912. <https://doi.org/10.1029/97JB00680>
- Salazar-Mora, C. A., Huisman, R. S., Fossen, H., & Eglydio-Silva, M. (2018). The Wilson Cycle and the effects of tectonic structural inheritance on rifted passive margin formation. *Tectonics*, 37, 3085–3101. <https://doi.org/10.1029/2018TC004962>
- Scisciani, V. (2009). Styles of positive inversion tectonics in the Central Apennines and in the Adriatic foreland: Implications for the evolution of the Apennine chain (Italy). *Journal of Structural Geology*, 31(11), 1276–1294. <https://doi.org/10.1016/j.jsg.2009.02.004>
- Scisciani, V., Agostini, S., Calamita, F., Pace, P., Cilli, A., Giori, I., & Paltrinieri, W. (2014). Positive inversion tectonics in foreland fold-and-thrust belts: A reappraisal of the Umbria–Marche Northern Apennines (Central Italy) by integrating geological and geophysical data. *Tectonophysics*, 637, 218–237. <https://doi.org/10.1016/j.tecto.2014.10.010>
- Scognamiglio, L., Tinti, E., Casarotti, E., Pucci, S., Villani, F., Cocco, M., Magnoni, F., et al. (2018). Complex fault geometry and rupture dynamics of the Mw 6.5, 2016, October 30th central Italy earthquake. *Journal of Geophysical Research: Solid Earth*, 123, 2943–2964. <https://doi.org/10.1002/2018JB015603>
- Selli, R. (1981). Thoughts on the geology of the Mediterranean region. In F. C. Wezel (Ed.), *Sedimentary Basin of Mediterranean Margins* (pp. 489–501). Tecnoprint, Bologna: C.N.R. Ital. Proj. Oceanography.
- Servizio Geologico d'Italia (1941). Carta Geologica d'Italia 1:100.000, Foglio 132 Norcia.
- Servizio Geologico d'Italia (1952). Carta Geologica d'Italia 1:100.000, Foglio 116 Gubbio.
- Servizio Geologico d'Italia (1955). Carta Geologica d'Italia 1:100.000, Foglio 139 L'Aquila.
- Servizio Geologico d'Italia (1958). Carta Geologica d'Italia 1:100.000, Foglio 125 Fermo.
- Servizio Geologico d'Italia (1963). Carta Geologica d'Italia 1:100.000, Foglio 140 Teramo.
- Servizio Geologico d'Italia (1965). Carta Geologica d'Italia 1:100.000, Foglio 118 Ancona.
- Servizio Geologico d'Italia (1966). Carta Geologica d'Italia 1:100.000, Foglio 117 Jesi.
- Servizio Geologico d'Italia (1967). Carta Geologica d'Italia 1:100.000, Foglio 124 Macerata.
- Servizio Geologico d'Italia (1968a). Carta Geologica d'Italia 1:100.000, Foglio 123 Assisi.
- Servizio Geologico d'Italia (1968b). Carta Geologica d'Italia 1:100.000, Foglio 131 Foligno.
- Servizio Geologico d'Italia (1969). Carta Geologica d'Italia 1:100.000, Foglio 133–34 Ascoli Piceno - Giulianova.
- Servizio Geologico d'Italia (1970). Carta Geologica d'Italia 1:100.000, Foglio 138 Terni.
- Storti, F., Balsamo, F., & Koopman, A. (2017). Geological map of the partially dolomitized Jurassic succession exposed in the core of the Montagna dei Fiori Anticline, Central Apennines, Italy. *Italian Journal of Geosciences*, 136(1), 125–135. <https://doi.org/10.3301/IJG.2016.05>
- Tavani, S., Storti, F., Bausà, J., & Muñoz, J. A. (2012). Late thrusting extensional collapse at the mountain front of the northern Apennines (Italy). *Tectonics*, 31, TC4019. <https://doi.org/10.1029/2011TC003059>
- Tavarnelli, E. (1997). Structural evolution of a foreland fold-and-thrust belt: The Umbria-Marche Apennines, Italy. *Journal of Structural Geology*, 19(3-4), 523–534. [https://doi.org/10.1016/S0191-8141\(96\)00093-4](https://doi.org/10.1016/S0191-8141(96)00093-4)
- Tavarnelli, E., Butler, R. W. H., Decandia, F. A., Calamita, F., Grasso, M., Alvarez, W., & Renda, P. (2004). Implications of fault reactivation and structural inheritance in the Cenozoic tectonic evolution of Italy. In U. Crescenti, S. D'Offizi, S. Merlini, & R. Sacchi (Eds.), (pp. 209–222). Italy: The Geology of Italy, Soc. Geol.
- Vai, G. B. (2001). Structure and stratigraphy: An overview. In G. B. Vai, & I. P. Martini (Eds.), *Anatomy of an Orogen: The Apennines and Adjacent Mediterranean Basins* (pp. 15–32). Dordrecht: Kluwer Academic Publ. [https://doi.org/10.1007/978-94-015-9829-3\\_3](https://doi.org/10.1007/978-94-015-9829-3_3)

- Valensise, G., & Pantosti, D. (2001). The investigation of potential earthquake sources in peninsular Italy: A review. *Journal of Seismology*, 5(3), 287–306. <https://doi.org/10.1023/A:1011463223440>
- Valensise, G., Vannoli, P., Basili, R., Bonini, L., Burrato, P., Carafa, M. M. C., et al. (2016). Fossil landscapes and youthful seismogenic sources in the central Apennines: Excerpts from the 24 August 2016, Amatrice earthquake and seismic hazard implications. *Annals of Geophysics*, 59(5). <https://doi.org/10.4401/ag-7215>
- Van Benthem, M. H., & Keenan, M. R. (2004). Fast algorithm for the solution of large-scale non-negativity-constrained least squares problems. *Journal of Chemometrics*, 18(10), 441–450. <https://doi.org/10.1002/cem.889>
- Vannoli, P., Burrato, P., Fracassi, U., & Valensise, G. (2012). A fresh look at the seismotectonics of the Abruzzi (Central Apennines) following the 6 April 2009 L'Aquila earthquake (Mw 6.3). *Italian Journal of Geosciences*, 131(3), 309–329. <https://doi.org/10.3301/IJG.2012.03>
- Vannoli, P., Burrato, P., & Valensise, G. (2015). The seismotectonics of the Po Plain (northern Italy): Tectonic diversity in a blind faulting domain. *Pure and Applied Geophysics*, 172(5), 1105–1142. <https://doi.org/10.1007/s00024-014-0873-0>
- Vannucci, G., & Gasperini, P. (2004). The new release of the database of earthquake mechanisms of the Mediterranean area (EMMA version 2). *Annales de Geophysique*, 47, 303–327.
- Vezzani, L., Festa, A., & Ghisetti, F. (2010). *Geology and tectonic evolution of the Central-Southern Apennines*, *Geol. Soc. Amer. Sp. Paper* (Vol. 469, p. 58).
- Vezzani, L., & Ghisetti, F. (1998). Carta geologica dell'Abruzzo, Scale 1:100,000, S.E.L.CA., Firenze.
- Villani, F., Civico, R., Pucci, S., Pizzimenti, L., Nappi, R., De Martini, P. M., & the Open EMERGE Working Group (2018). A database of the coseismic effects following the 30 October 2016 Norcia earthquake in Central Italy. *Scientific Data*, 5, 180049. <https://doi.org/10.1038/sdata.2018.49>
- Walters, R. J., Gregory, L. C., Wedmore, L. N. J., Craig, T. J., McCaffrey, K., Wilkinson, M., et al. (2018). Dual control of fault intersections on stop-start rupture in the 2016 Central Italy seismic sequence. *Earth and Planetary Science Letters*, 500, 1–14. <https://doi.org/10.1016/j.epsl.2018.07.043>
- Wang, L., Gao, H., Feng, G., & Xu, W. (2018). Source parameters and triggering links of the earthquake sequence in central Italy from 2009 to 2016 analyzed with GPS and InSAR data. *Tectonophysics*, 744, 285–295. <https://doi.org/10.1016/j.tecto.2018.07.013>
- Westaway, R. (1999). The mechanical feasibility of low-angle normal faulting. *Tectonophysics*, 308(4), 407–443. [https://doi.org/10.1016/S0040-1951\(99\)00148-1](https://doi.org/10.1016/S0040-1951(99)00148-1)
- Xu, G., Xu, C., Wen, Y., & Jiang, G. (2017). Source parameters of the 2016–2017 Central Italy earthquake sequence from the Sentinel-1, ALOS-2 and GPS data. *Remote Sensing*, 9(11), 1182. <https://doi.org/10.3390/rs9111182>
- Zhong, S., Xu, C., Yi, L., & Li, Y. (2018). Focal mechanisms of the 2016 Central Italy earthquake sequence inferred from high-rate GPS and broadband seismic waveforms. *Remote Sensing*, 10(4), 512. <https://doi.org/10.3390/rs10040512>